



**UNIVERSIDAD DE INVESTIGACIÓN DE
TECNOLOGÍA EXPERIMENTAL YACHAY**

Escuela de Ciencias Químicas e Ingeniería

**Evaluation of adsorbent capacity of magnetite-chitosan
nanocomposites hydrogels against environmental pollutant
compounds.**

Trabajo e integración curricular presentado como requisito para la
obtención del título de Polímeros

Autor:

Pablo Andrés Carrión Martínez

Tutor:

Ph.D. Rose Mary Michell

Co-Tutor

Ph.D. Floralba López

Urququí, octubre 2021

SECRETARÍA GENERAL
(Vicerrectorado Académico/Cancillería)
ESCUELA DE CIENCIAS QUÍMICAS E INGENIERÍA
CARRERA DE POLÍMEROS
ACTA DE DEFENSA No. UITEY-CHE-2022-00023-AD

A los 21 días del mes de enero de 2022, a las 14:00 horas, de manera virtual mediante videoconferencia, y ante el Tribunal Calificador, integrado por los docentes:

Presidente Tribunal de Defensa	Mgs. DE LIMA ELJURI, LOLA MARIA
Miembro No Tutor	Dra. GONZALEZ VAZQUEZ, GEMA , Ph.D.
Tutor	Dra. MICHELL URIBE, ROSE MARY RITA , Ph.D.

El(la) señor(ita) estudiante **CARRION MARTINEZ, PABLO ANDRES**, con cédula de identidad No. **1150269106**, de la **ESCUELA DE CIENCIAS QUÍMICAS E INGENIERÍA**, de la Carrera de **POLÍMEROS**, aprobada por el Consejo de Educación Superior (CES), mediante Resolución **RPC-SO-41-No.476-2014**, realiza a través de videoconferencia, la sustentación de su trabajo de titulación denominado: **Evaluation of adsorbent capacity of magnetite-chitosan nanocomposites hydrogels against environmental pollutant compounds.**, previa a la obtención del título de **INGENIERO/A DE POLÍMEROS**.

El citado trabajo de titulación, fue debidamente aprobado por el(los) docente(s):

Tutor	Dra. MICHELL URIBE, ROSE MARY RITA , Ph.D.
Co - Tutor	Dra. LOPEZ GONZALEZ, FLORALBA AGGENY , Ph.D.

Y recibió las observaciones de los otros miembros del Tribunal Calificador, las mismas que han sido incorporadas por el(la) estudiante.

Previamente cumplidos los requisitos legales y reglamentarios, el trabajo de titulación fue sustentado por el(la) estudiante y examinado por los miembros del Tribunal Calificador. Escuchada la sustentación del trabajo de titulación a través de videoconferencia, que integró la exposición de el(la) estudiante sobre el contenido de la misma y las preguntas formuladas por los miembros del Tribunal, se califica la sustentación del trabajo de titulación con las siguientes calificaciones:

Tipo	Docente	Calificación
Tutor	Dra. MICHELL URIBE, ROSE MARY RITA , Ph.D.	9,0
Presidente Tribunal De Defensa	Mgs. DE LIMA ELJURI, LOLA MARIA	10,0
Miembro Tribunal De Defensa	Dra. GONZALEZ VAZQUEZ, GEMA , Ph.D.	9,0

Lo que da un promedio de: **9.3 (Nueve punto Tres)**, sobre 10 (diez), equivalente a: **APROBADO**

Para constancia de lo actuado, firman los miembros del Tribunal Calificador, el/la estudiante y el/la secretario ad-hoc.

Certifico que *en cumplimiento del Decreto Ejecutivo 1017 de 16 de marzo de 2020, la defensa de trabajo de titulación (o examen de grado modalidad teórico práctica) se realizó vía virtual, por lo que las firmas de los miembros del Tribunal de Defensa de Grado, constan en forma digital.*

CARRION MARTINEZ, PABLO ANDRES
Estudiante

Mgs. DE LIMA ELJURI, LOLA MARIA
Presidente Tribunal de Defensa



Firmado electrónicamente por:
LOLA MARIA
DE LIMA

ROSE MARY RITA
 MICHELL URIBE

Firmado digitalmente por ROSE
 MARY RITA MICHELL URIBE
 Fecha: 2022.01.24 09:09:36 -05'00'

Dra. MICHELL URIBE, ROSE MARY RITA , Ph.D.
Tutor

GEMA GONZALEZ VAZQUEZ Digitally signed by GEMA
GONZALEZ VAZQUEZ
Date: 2022.01.21
21:05:10 -05'00'

Dra. GONZALEZ VAZQUEZ, GEMA , Ph.D.
Miembro No Tutor

YEPEZ MERLO, MARIELA SOLEDAD
Secretario Ad-hoc



Firmado electrónicamente por:
**MARIELA
SOLEDAD YEPEZ
MERLO**

AUTORÍA

Yo, PABLO ANDRÉS CARRIÓN MARTÍNEZ, con cédula de identidad 1150269106, declaro que las ideas, juicios, valoraciones, interpretaciones, consultas bibliográficas, definiciones y conceptualizaciones expuestas en el presente trabajo; así cómo, los procedimientos y herramientas utilizadas en la investigación, son de absoluta responsabilidad de el autor del trabajo de integración curricular. Así mismo, me acojo a los reglamentos internos de la Universidad de Investigación de Tecnología Experimental Yachay.

Urcuquí, octubre 2021

Pablo Andrés Carrión Martínez

CI: 1150269106

AUTORIZACION DE PUBLICACIÓN

Yo, PABLO ANDRÉS CARRIÓN MARTÍNEZ, con cédula de identidad 1150269106, cedo a la Universidad de Tecnología Experimental Yachay, los derechos de publicación de la presente obra, sin que deba haber un reconocimiento económico por este concepto. Declaro además que el texto del presente trabajo de titulación no podrá ser cedido a ninguna empresa editorial para su publicación u otros fines, sin contar previamente con la autorización escrita de la Universidad.

Asimismo, autorizo a la Universidad que realice la digitalización y publicación de este trabajo de integración curricular en el repositorio virtual, de conformidad a lo dispuesto en el Art. 144 de la Ley Orgánica de Educación Superior.

Uruguay, octubre 2021

Pablo Andrés Carrión Martínez

CI: 1150269106

Dedication

To my mom Eunice and brothers

Acknowledgments

First of all, I would like to thank my mother Eunice Martinez for her special support, love and strength throughout my college career. Her help, effort and life example has served me as a reference to face the challenges presented in the academy and achieve the objectives planted in my personal goals. I also wish to express my special gratitude to my advisor Ph. D. Rose Mary Michell, and my co-advisor Ph. D. Floralba Lopez for their invaluable support, guidance and patience during the development of this research work. I want them to know that they are my professional references and that I greatly admire their dedication and devotion to the research. I would also like to express my sincere thanks to Professor Alexis Debut and Eng. Karla Vizuite from Espe's Electron Microscopy Center for their collaboration in the SEM and TEM tests. Finally, I would also like to thank my professors throughout my career, for their excellence and dedication, my friends for being part of my life and who I am now, and my family because I do not know if I would have gotten to where I am now without them.

TITLE: Evaluation of magnetite-chitosan nanocomposites hydrogels

ABSTRACT:

In this study, magnetic chitosan (CS)-based hydrogel nanocomposites were characterized via SEM, TEM, XPS, FTIR for the samples' morphological, structural, and compositional analysis, and swelling tests for the analysis of the maximum swelling degree. Magnetic CS-based hydrogel nanocomposites resulted in having a regular and well-defined porous structure, with spherical magnetic nanoparticles embedded in the chitosan matrix. Deconvolution peaks obtained by XPS analyses and stretching vibrations in the FTIR studied spectra on magnetic CS-based hydrogel nanocomposites confirm chelate formations between iron ions and amino and hydroxyl groups from chitosan. On the other hand, swelling experiments resulted in swelling percentage values between 600 % to 1300 % approximately at pH 7 and room temperature for two hours, depending on external condition variations (pH, temperature). Finally, the obtained adsorption experiments concluded a 1.811 $\mu\text{mol/mg}$ maximum adsorption quantity of Chromium (Cr^{6+}) at standard conditions (pH 7, Temp 25 $^{\circ}\text{C}$) for 24 hr in the magnetic CS-based hydrogel nanocomposites. Adsorption follows a pseudo-second-order kinetic and a Redlich-Peterson isotherm model with a predominance behavior of the Langmuir model, showing that the adsorption type follows non-ideal monolayer adsorption. The results demonstrated a good performance of magnetic CS-based hydrogels nanocomposites on the adsorption of chromium metal ions from aqueous solutions and their potential uses for waste-water treatment.

Keywords: CS-based hydrogel, nanocomposite, magnetite, crosslinker, glutaraldehyde, wastewater

TÍTULO: Evaluación de hidrogeles nanocompuestos de quitosano y magnetita

RESUMEN:

En este estudio, los hidrogeles nanocompuestos magnéticos basados en quitosano (CS) se caracterizaron mediante SEM, TEM, XPS, FTIR para el análisis morfológico, estructural y de composición de las muestras, y mediante pruebas de hinchamiento para el análisis del grado máximo de hinchamiento. Los hidrogeles nanocompuestos magnéticos basados en CS resultaron tener una estructura porosa regular y bien definida, con nanopartículas magnéticas esféricas incrustadas en una matriz de quitosano. Los picos de desconvolución obtenidos por los análisis XPS y las vibraciones de estiramiento en los espectros estudiados de FTIR en los hidrogeles nanocompuestos magnéticos basados en CS confirman la formación de quelatos dado entre los iones de hierro y los grupos amino e hidroxilo del quitosano. Por otra parte, los experimentos de hinchamiento dieron como resultado valores de porcentaje de hinchamiento entre el 600 % y el 1300 % aproximadamente a pH 7 y temperatura ambiente durante dos horas, dependiendo de las variaciones de las condiciones externas (pH, temperatura). Por último, los experimentos de adsorción realizados concluyen que la cantidad máxima de adsorción de cromo (Cr^{6+}) por los hidrogeles nanocompuestos magnéticos basados en CS, es de aproximadamente 1,811 $\mu\text{mol/mg}$ en condiciones estándar (pH 7, temperatura 25 °C) durante 24 horas. La adsorción sigue una cinética de pseudo-segundo orden y un modelo de isoterma de Redlich-Peterson con un comportamiento predominante del modelo de Langmuir, mostrando que el tipo de adsorción sigue una adsorción monocapa no ideal. Los resultados demostraron un buen rendimiento de los hidrogeles nanocompuestos magnéticos a base de CS en la adsorción de iones metálicos de cromo a partir de soluciones acuosas y sus usos potenciales para el tratamiento de aguas residuales.

Palabras clave: Hidrogeles basados en quitosano, nanocompositos, magnetita, entrecruzante, gluteraldehído, aguas residuales.

INDEX

1	INTRODUCTION.....	I
2	BACKGROUND:	IV
2.1	Hydrogels.....	IV
2.2	Mechanisms of hydrogel formation.....	IV
2.2.1	Chemically Crosslinking Hydrogels.....	IV
2.2.2	Physically synthesized hydrogels	VI
2.3	Chitosan; properties, advantages, and some applications.....	VII
2.4	Glutaraldehyde on chitosan hydrogel beads	VIII
2.5	Magnetite influence on adsorption and desorption capacities of chitosan hydrogel beads	X
2.6	Adsorption Mechanisms	X
2.6.1	Henry`s Isotherms.	XI
2.6.2	Langmuir adsorption isotherm.....	XI
2.6.3	Freundlich adsorption isotherm.....	XII
2.6.4	Temkin adsorption isotherm.....	XII
2.6.5	Redlich-Peterson isotherm model.....	XII
2.7	Adsorption Kinetic Studies	XIII
2.7.1	Pseudo-First-Order Kinectic Model	XIII
2.7.2	Pseudo-Second-Order Kinetic Model.....	XIV
2.7.3	Intraparticle Diffusion Model.....	XIV
2.8	Thermodynamic Adsorption Studies	XV
3	PROBLEM STATEMENT	XVI
4	OBJECTIVES	XVII
4.1	4.1 General Objective	XVII
4.2	4.2 Specific Objectives	XVII
5	METHODOLOGY	XVIII
5.1	Materials	XVIII
5.2	Experimental Description	XIX
5.2.1	Morphological and structural analysis.....	XIX

5.2.2	Chemical composition analysis	XIX
5.2.3	Swelling capacity studies	XX
5.2.4	Ultraviolet-visible spectroscopy characterization for adsorption analysis ..	XXI
6	RESULTS AND DISCUSSION	XXIII
6.1	Morphological and structural analysis of CS-Based Hydrogel Nanocomposites XXIII	
6.1.1	Scanning Electron Microscopy (SEM) analysis	XXIII
6.1.2	Transmission Electron Microscopy (TEM) analysis	XXIV
6.2	Chemical composition studies of CS-Based Hydrogel Nanocomposites	XXVI
6.2.1	X-Ray Photoelectron Spectroscopy (XPS) analysis	XXVI
6.2.2	Fourier-Transformed Infrared Spectroscopy (FTIR) analysis	XXXIII
6.3	Swelling analysis of CS-Based Hydrogel Nanocomposites.	XXXIV
6.4	Adsorption Analysis	XXXVIII
6.4.1	Adsorption of Chromium (Cr ⁶⁺) on CS-based hydrogel nanocomposites XXXVIII	
6.4.2	Chromium (Cr ⁶⁺) adsorption kinetic studies	XLII
6.4.3	Chromium (Cr ⁶⁺) adsorption equilibrium studies.....	XLV
6.4.4	Chromium (Cr ⁶⁺) adsorption thermodynamic studies	L
7	CONCLUSIONS.....	LII
8	BIBLIOGRAPHY:.....	LIV

LIST OF FIGURES

- Figure 1.** Chemical structure of chitosan chemically cross-linked with glutaraldehyde [55]. IX
- Figure 2.** SEM images from samples prepared by drip method a) Q_D, b) Q_DX_{0.35}, c) Q_DX_{0.75}, d) Q_DM, e) Q_DX_{0.35}M, f) and Q_DX_{0.75}M samples. XXIV
- Figure 3.** TEM images from samples prepared by drip method a) Q_D, b) Q_DX_{0.35}, c) Q_DX_{0.75}, d) Q_DM, e) Q_DX_{0.35}M, f) and Q_DX_{0.75}M samples. XXV
- Figure 4.** XPS spectra of the survey XPS spectra from Q_D, Q_DM, Q_DX_{0.75}M sample. XXVII
- Figure 5.** XPS spectra of C1s from a) Q_D, b) Q_DX_{0.35}, c) Q_DX_{0.75}, d) Q_DM, e) Q_DX_{0.35}M, and f) Q_DX_{0.75}M samples. XXVIII
- Figure 6.** XPS spectra of O1s from a) Q_D, b) Q_DX_{0.35}, c) Q_DX_{0.75}, d) Q_DM, e) Q_DX_{0.35}M, and f) Q_DX_{0.75}M samples. XXIX
- Figure 7.** XPS spectra of N1s from a) Q_D, b) Q_DX_{0.35}, c) Q_DX_{0.75}, d) Q_DM, e) Q_DX_{0.35}M, and f) Q_DX_{0.75}M sample. XXX
- Figure 8.** XPS spectra of Fe 2p from a) Q_D, b) Q_DX_{0.35}, c) Q_DX_{0.75}, d) Q_DM, e) Q_DX_{0.35}M, and f) Q_DX_{0.75}M sample. XXXI
- Figure 9.** FTIR spectra of the CS-based hydrogel nanocomposites for a) Q_D, b) Q_DX_{0.35}, c) Q_DX_{0.75}, and d) Q_DX_{0.75}M samples. XXXIV
- Figure 10.** Swelling kinetics of chitosan hydrogels at pH 7 for Q_D, Q_DX_{0.35}, Q_DX_{0.75}, Q_DM, Q_DX_{0.35}M, and Q_DX_{0.75}M samples, at room temperature. XXXVI
- Figure 11.** pH-dependency swelling of Q_D, Q_DX_{0.35}, Q_DX_{0.75}, Q_DM, Q_DX_{0.35}M, and Q_DX_{0.75}M samples at room temperature. XXXVII
- Figure 12.** Temperature dependency swelling of Q_D, Q_DX_{0.35}, Q_DX_{0.75}, Q_DM, Q_DX_{0.35}M, and Q_DX_{0.75}M s at pH 7. XXXVIII
- Figure 13.** Effect of initial concentration on the Cr⁶⁺ adsorption experiments on Q_DX_{0.35}, Q_DX_{0.75}, Q_DX_{0.35}M, and Q_DX_{0.75}M samples at 25 °C and 25 hours of exposure. XXXIX
- Figure 14.** Effect of temperature and contact time on Q_DX_{0.75}M samples in the adsorption of Cr⁶⁺ solution at 300 ppm. XLII
- Figure 15.** Pseudo first and pseudo second order kinetic plots for Cr⁶⁺ adsorption on Q_DX_{0.75}M samples at a) 25 °C, b) 35 °C and c) 45 °C. XLIII
- Figure 16.** Intraparticle diffusion plots at different temperatures for Cr⁶⁺ adsorption on Q_DX_{0.75}M samples. XLV

Figure 17. Langmuir isotherm plots for Cr⁶⁺ adsorption of Q_DX_{0.75}M samples at a) 25 °C, b) 35 °C and c) 45 °C. XLVII

Figure 18. Freundlich isotherm plots for Cr⁶⁺ adsorption of Q_DX₇₅M samples at a) 25 °C, b) 35 °C and c) 45 °C. XLVIII

Figure 19. Redlich-Peterson isotherm plots for Cr⁶⁺ adsorption of Q_DX₇₅M samples at a) 25 °C, b) 35 °C, and c) 45 °C. XLVIII

Figure 20. Temkin isotherm plots for Cr⁶⁺ adsorption of Q_DX₇₅M samples at a) 25°C, b) 35°C and c) 45°C..... XLIX

LIST OF TABLES

- Table 1.** Total heavy metal concentrations ($\mu\text{g L}^{-1}$) and selected sample numbers (SN) of the global river and lake water bodies from the 1970s to the 2010s, and concentrations of heavy metals in water as per World Health Organization (WHO) and the United States Environmental Protection Agency (USEPA) standards [5].I
- Table 2.** Nomenclature of the CS-based hydrogel nanocomposites used in this work. XVIII
- Table 3.** “q” values obtained from different Solution volume: Hydrogel weight ratios of the $\text{Q}_\text{D}\text{X}_{0.75}\text{M}$ sample in the adsorption of Cr^{6+}XL
- Table 4.** “q” values obtained from different pH solution in the adsorption of Cr^{6+} by $\text{Q}_\text{D}\text{X}_{0.75}\text{M}$ sample at room temperature: XLI
- Table 5.** Kinetic parameters for Cr^{6+} adsorption on $\text{Q}_\text{D}\text{X}_{0.75}\text{M}$ samples at 25 °C, 35 °C and 45 °C. XLIV
- Table 6.** Intraparticle diffusion constants calculated at different temperatures for Cr^{6+} adsorption on $\text{Q}_\text{D}\text{X}_{0.75}\text{M}$ samples. XLV
- Table 7.** Isotherm constants from Langmuir, Freundlich, Temkin, and Redlich-Peterson models at different temperatures, obtained from Cr^{6+} adsorption on $\text{Q}_\text{D}\text{X}_{75}\text{M}$ samples. XLIX
- Table 8.** Separation factor from Langmuir Models at different temperatures.....L
- Table 9.** Thermodynamic parameters for Chromium (Cr^{6+}) adsorption into $\text{Q}_\text{D}\text{X}_{75}\text{M}$ samples. L

ABREVIATIONS

CS Chitosan

SEM Scanning electron microscopy

TEM Transmission electron microscopy

XPS X-Ray photoelectron spectroscopy

FTIR Fourier transform infrared spectroscopy

GLA Glutaraldehyde

UV Ultra-violet

q_m Amount of maximum metal ions adsorbed on the adsorbent

q_e Amount of metal ions adsorbed at the equilibrium on the adsorbent

C_e Concentration of the metal on the solution at the equilibrium

1 INTRODUCTION

Toxic metal pollution in global water, rivers, and oceans has become a significant concern for all governments and countries worldwide. The primary resources of these toxic metals are natural resources such as rock weathering, volcanic eruption, sea-salt sprays between others and anthropogenic resources in which processes interfere the human being, such as Industrial activities, agriculture, waste-water, mining, metallurgical process, between others [1-3]. Many of the toxic metals, product of these activities, finally end up over the environmental surface and waters from urban areas [4]. There exist a reported trend, shown in *Table 1*, of increasing concentration of toxic metals such as Fe, Mn, Ni, Cu, Cr, and Cd over rivers and lakes around the world from 1970 to 2017; being between 1990, 2000, and 2010 the years where toxic metals were founded at higher concentrations compared to the 1970s and 1980s [5]. In addition, the concentration of toxic metals varies over the five continents being Africa, Asia, and South America, where the higher concentrations of toxic metal in rivers and lakes were found and lower in Europe and North America [5].

Table 1. Total heavy metal concentrations ($\mu\text{g L}^{-1}$) and selected sample numbers (SN) of the global river and lake water bodies from the 1970s to the 2010s, and concentrations of heavy metals in water as per World Health Organization (WHO) and the United States Environmental Protection Agency (USEPA) standards [5].

<i>Metals</i>	<i>1970s</i>	<i>2000s</i>	<i>2010s</i>	<i>Standars</i>	
	<i>Mean ± S.E.</i>	<i>Mean ± S.E.</i>	<i>Mean ± S.E.</i>	<i>WHO</i>	<i>USEPA</i>
<i>Cd</i>	0.82 ± 0.18	21.60 ± 6.42	25.33 ± 7.17	3	5
<i>Cr</i>	----	641.45 ± 414.89	138.47 ± 53.18	50	100
<i>Cu</i>	5.91 ± 1.58	433.636 ± 307.86	119.98 ± 39.32	2000	1300
<i>Ni</i>	1.43 ± 0.16	59.98 ± 27.08	80.99 ± 26.55	20	----
<i>Mn</i>	444.89 ± 290.92	894.36 ± 3574.51	518.00 ± 221.69	100	50
<i>Fe</i>	967.14 ± 693.83	2852.61 ± 1636.45	1479.55 ± 420.04	300	300

Toxic metal concentrations on global water resources are the cause of many health issues and irreversible environmental damage. In the 1970s, 2000s, and 2010, the cancer risks related to Cr content in surface water went beyond the permissible limit; Asia, África, and North America were the main continents with this problem [6]. Prolonged exposure to Cr may lead to a high probability of contracting cancer by dermal contact, oral ingestion, or inhalation [7].

To avoid the possible health risks and environmentally toxic metal pollution of worldwide rivers and lakes is necessary to develop new alternatives to control the high levels of toxic metals in water. In this aspect, new water treatment methods have been developed to get ridding of such metal ions like; chemical precipitation, membrane filtration, flotation, coagulation-flocculation, ion-exchange, adsorption, and electrochemical methods [8] being adsorption the best choice because of its efficiency, its simplicity and low production costs [9]. In this context, hydrogels properties seem to be an efficient option to be applied as an adsorption agent for different metal ions in aqueous solutions. The study of hydrogels based on polymers with crosslinking networks has focused on improving the super-adsorbent capabilities by retaining and releasing metal ion contaminants present in aqueous media at different environmental conditions. Incorporating inorganic compounds such as activated carbon, graphene, nanoparticles, and crosslinkers in different natural polymers such as chitosan, cellulose, alginate, and collagen has allowed enhancing the adsorption capacity and improving the mechanical and physicochemical properties of hydrogels [10]. Lately, these materials have received much attention in water and waste-water processes, especially chitosan-based hydrogels, which have metal chelation and dye removal properties [11,12]. Chitosan, as an ecofriendly adsorbent, has a low-cost production; it is renewable, non-toxic, biodegradable, hydrophilic, and has high reactivity coagulation, flocculation, and biosorption properties due to its hydroxyl and amine groups in its macromolecular chains [13-15]. Chitosan hydrogels have good swelling properties, maintaining their original shape without dissolving in water. Investigations about the incorporation of inorganic materials have focused on the thermal stability and mechanical resistance to improve the properties of chitosan hydrogels [16-18]. By modifying chitosan hydrogels, the swelling and adsorption capacities can be adapted in response to different environments, including pH, temperature, ionic strength, and initial concentrations of the adsorbate [19].

Researches have been made on chitosan composites preparation to improve further their properties, such as the preparation of thiourea/chitosan composite beads for the removal of copper(II) from aqueous solutions higher adsorption capacities in the surface of the beads despite their low pore size distribution [20]. Another example is the preparation of the biodegradable chitosan-coated sand (CCS) tested in the removal of Cu (II) and Pb (II) ions in water. The amount of adsorbed metal ions resulted higher for Pb(II) than for Cu (II) at

higher pH values, resulting in better bonding strength and stability under neutral conditions[21]. On the other hand, a novel chitosan/ clinoptilolite composite was synthesized and evaluated in the Cu^{2+} , Co^{2+} , and Ni^{2+} , with better adsorption values for Cu^{2+} Ni^{2+} and indicating spontaneity on the adsorption process, following a pseudo-second-order equation, and fitting a Langmuir plot which better describes the adsorption process [22]. However, investigations are still in progress to prepare chitosan composites to improve their efficiency in removing toxic pollutants, improving their mechanical and physical properties, and their adsorption capacities.

In the present thesis project, the characterization and adsorption properties of chitosan-magnetite nanocomposite hydrogels are evaluated for Chromium (Cr^{6+}) adsorption at different concentrations, contact times, pH, and temperature values. Chitosan-magnetite nanocomposite hydrogels were previously synthesized by drip and solvent evaporated methods in the “Chitosan-based hydrogel for waste-water treatment” thesis project. Scanning electron microscopy, X-ray diffraction, and thermogravimetric characterizations made by the mentioned thesis project concluded on good thermal stability, regular and defined pore sizes, and confirmed the magnetite particles in the chitosan-hydrogel structure [23]. The current thesis project pretends to be a continuation of the work made “Chitosan-based hydrogel for waste-water treatment” thesis project with the characterization via Transmission electron microscopy (TEM), X-ray diffraction analysis (XRD), Fourier transform infrared spectrometry (FTIR), and swelling degree determination of the magnetic and non-magnetic CS-based hydrogel nanocomposites synthesized by the drip method. Finally, kinetic, isothermal, and thermodynamic studies were developed, and the effects of pH, temperature, contact time, and initial metal concentration were evaluated in the adsorption capacity of the samples in Chromium (Cr^{6+}) solutions.

2 THEORETICAL BACKGROUND:

2.1 Hydrogels

Hydrogels are polymeric structures connected by either ionic forces, primary covalent crosslinks, hydrogen bonds, hydrophobic interactions, physical entanglements, or the combination of any of the mentioned interactions [24]. Hydrogels are considered two or more multicomponent polymeric systems of a three-dimensional structure, with the capacity of swelling but not dissolve in water [25]. The swelling water ability of hydrogels can be explained by the hydrophilic functional groups present in their polymeric network, such as –NH₂, –COOH, –OH, –CONH₂, CONH, and SO₃H, and their dissolution resistance depend on their existing crosslinks between polymer chains [26]. Hydrogels go through a significant volume phase transition, or gel-sol phase transition, when they are exposed to physical or chemical stimuli such as temperature, electric or magnetic fields, solvent compositions, and even to pH changes, ions, and specific chemical compositions. Many of these changes are reversible and depend on the nature of the monomer, charge density, degree of cross linkage, among others [27].

Due to their properties, hydrogels have been studied for many biomedical and engineering applications, starting on tissue-engineering scaffolds, soft contact lenses, sensors, actuators, drug delivery systems, antifouling coatings, soft robotics, and waste-water treatment [28, 29].

2.2 Mechanisms of hydrogel formation.

Principally, hydrogels can be formed by two types of reaction mechanisms. Depending on their specific application, hydrogels are synthesized by either chemical crosslinking or physical crosslinking.

2.2.1 Chemically Crosslinking Hydrogels

In the chemical crosslinking method, polymer chains on hydrogels are attached by covalent bonds product of chemical reactions of complementary functional groups, such as

chemical reactions between polymer chains inside the hydrogel or between polymer chains and cross-linkers, reactions by chemical grafting, and by free-radical polymerization [28].

2.2.1.1 Chemical crosslinking via reaction of complementary functional groups

These types of reactions are found via amine-carboxylic acid or isocyanate OH/NH₂ groups, used for establishing covalent bonds between diverse monomeric and polymeric chains [30]. Reactions involving hydrophilic –OH groups such as polyvinyl alcohol can be crosslinked with glutaraldehyde [31]. Aldehyde crosslinking. Additionally, polymers involving amine and ester moieties groups resulting in Schiff base formation via condensation crosslinking, and polymers with higher functional crosslinkers react via addition reactions with multifunctional groups [32, 33].

2.2.1.2 Chemical crosslinking via chemical grafting reactions

Chemical crosslinking via grafting different functional groups such as amino–NH₂, carboxyl –COOH, acylamino –CONH₂, and sulphonic –SO₃H groups to the backbone of hydrogel polymers. These grafting reactions increase the adsorption efficiency by increasing the number of sorption sites, polarity surface, and hydrophilicity [34]. In this field, polysaccharide polymers grafted with vinyl groups have been studied, resulting in additional thermal stability and turnover over the solid polymer matrix compared to the hydrogel without any grafting [35].

2.2.1.3 Chemical crosslinking via free radical polymerization

In this chemical crosslinking, a free radical generating chemical compound starts by decomposition factors like redox reaction, temperature, light, and ultraviolet radiation. The resulting product undergoes a formation and propagation process of the polymeric chains. In these steps, the crosslinking of the polymeric chain develops a three-dimensional network in the polymeric structure [36].

2.2.2 Physically synthesized hydrogels

In the physically crosslinked hydrogels, the intermolecular interactions of the polymer chains are given by strong/weak forces such as electrostatic interactions, hydrogen bonds, hydrophobic interactions, crystallization, among others. The synthesis occurs under mild conditions, and no cross-linkers are involved.

2.2.2.1 Physical synthesis via hydrogel bonds

Polymer chains can be crosslinked by multiple hydrogen bonds between hydrogen linked to an electronegative atom like N, O, F, and another electronegative atom with free electron pairs. For instance, Zhang et al. synthesized an ABA triblock thermoresponsive copolymer containing ureidopyrimidinone (UPy) functionalized monomers. The polymer structure formation was formed by the quadruple hydrogen bonds formed between UPy groups. These polymer structures have excellent injectable and self-healing properties applied on 3D cell encapsulation for drug delivery applications [37, 28].

2.2.2.2 Physical synthesis via electrostatic interactions

Polymers can be synthesized by electrostatic interactions between complementary ionic polypeptides, oppositely charged polyelectrolytes, negatively charged polyanions, or multivalent cations [28].

2.2.2.3 Physical synthesis via hydrophobic interactions

Hydrogel polymers bonded through hydrophobic interactions have been applied for biological and engineering processes, such as biomolecular complexation, flotation, protein folding, oil and sand extraction, among others [38]. Some examples of this kind of polymers are amphiphilic block copolymers, poly(N-substituted acrylamide)-based and poly(vinyl ether)-based block copolymers, grafted copolymers. After a heating process, dehydrated and hydrophobic blocks form hydrophobic interactions acting as the crosslinks of the hydrogel [28].

2.2.2.4 Physical synthesis via crystallization.

The polymeric structure undergoes a freezing-thawing process in the physical synthesis via crystallization method, resulting in harsh and highly elastic hydrogels. Poly(vinyl alcohol) PVA hydrogels are synthesized by this method [33]. In the freezing process, PVA chains concentrate, and crystallization occurs due to hydrogen bonds generated between the PVA chains. After the thawing process, the crystalline regions of PVA remain unchanged, becoming the physical crosslinks of the PVA, resulting in better mechanical properties and biocompatibility for the hydrogel [28, 39].

2.3 Chitosan; properties, advantages, and some applications

Chitosan, whose structure is based on D-glucosamine attached to N-acetyl D-glucosamine by β -1,4-glycosidic bond, originates from deacetylation of chitin biopolymer extracted from shellfish sources [40]. It is a linear hydrophilic amino polysaccharide with glucosamine and acetyl glucosamine units in its structure. Each glucosamine unit presents reactive amino and hydroxyl groups, as shown in *Figure 1*, making chitosan useful for many industrial applications [41]. Properties like biodegradability, biocompatibility, low toxicity, different biological activities, and good adsorption make chitosan a valuable material for further research about improving their physical, chemical, and mechanical properties [42].

Chitosan is founded on mushrooms, cell walls of fungi, yeasts, and many marine shellfish such as crabs, shrimps, lobsters, squid pens, and cuttlefish, forming the outer shell by covalently bound with proteins, carotenoids, and metals [40,42]. For industrial production and commercial applications, the primary resources of chitosan are shrimp, prawn, and crab wastes obtained from aquaculture and fishing activities [42, 43].

Chitosan production derived from crustacean shells has four central unit operations: demineralization, deproteinization, decoloration, and deacetylation. This last step involves deacetylation of chitin in 40% sodium hydroxide for approximately 3 hours and a temperature of 120 °C, resulting in 70 % deacetylated chitosan [44]. Optimization studies have been made for deacetylation on chitosan production, resulting in polymer's molecular weight response surface methodology. Varying temperature and time, an estimate of chitosan's intrinsic viscosity was measured by linear regression adapting the Huggins Houwink-Sakurada

method. With optimal temperature and time of 130°C and 90 min, respectively, a deacetylation degree of 90% was obtained in the process of chitosan production [45].

Chitosan has been widely used for agriculture, medicine, chemistry, food processing, biotechnology, environmental engineering, among others [42, 46]. In this last one, especially in the water treatment field, chitosan has been studied for its characteristic static attraction and adsorption of metal ions and toxic dyes potentially found on waste-water effluents. Compared to chitin, chitosan presents superior metal ion adsorption ability due to its amino and hydroxyl groups, which form chelates between metal ions and chitosan depending on the nature of the cation [47].

To remove toxic metal ions and dyes from waste water, studies on developing chitosan hydrogels have increased in the last years, getting good results in the adsorption capacities of chitosan hydrogels but showing some drawbacks such as low strength in some acidic mediums, low mechanical properties, and thermal stability. To solve these problems, the use of chemical and physical networking methods such as crosslinking, grafting, impregnation of rigid fillers, and blending, among other [48], has been investigated being, the use of glutaraldehyde and magnetic nanoparticles, the focus of interest on this thesis project.

2.4 Glutaraldehyde on chitosan hydrogel beads

Crosslinking on chitosan hydrogels can be done by physical and chemical networking methods. In the physical networking method, the physical bond is reversible and based on molecular entanglements, ionic interactions, and hydrogen bonding. In this context, anionic crosslinkers commonly used are tripolyphosphate, sodium citrate, sulfosuccinate acid, among others [21]. On the other hand, chemical networking consists of irreversible covalent bonds in a chemical reaction between crosslinkers and the polymer chains. These chemical agents can be N,N'-methylenebisacrylamide, ethylene glycol diglycidyl ether, epichlorohydrin, glutaraldehyde, among others [48]. Because of the nature of the covalent bonds, chemical crosslinking gives more stability and cohesion capacities to the hydrogels than physical crosslinked bonds.

Chitosan becomes vulnerable when it is in contact with acidic solutions, dissolving itself and losing its property of binding sorbates [49,50]. In order to solve this problem, hydrogels

crosslinked with glutaraldehyde are used to enhance the stability of the structure by increasing its mechanical properties and decreasing its solubility when it is in contact with an acidic medium. Glutaraldehyde has active aldehyde groups, which can be crosslinked with chitosan by the formation of Schiff's base when the nitrogen from the amino group of chitosan makes a nucleophilic attack on the carbon from the glutaraldehyde molecule [51], resulting in crosslinked chitosan with glutaraldehyde as is shown in **Figure 1**.

In addition to improving mechanical resistance and stable sorbent properties in an acidic medium, glutaraldehyde crosslinker does not seem to affect the regeneration properties of the hydrogel beads. Desorption studies of AR37 dye from chitosan, chitosan-GLA, and chitosan- H₂SO₄ beads showed a high desorption value in all the cases, confirming the type of adsorption via electrostatic attraction. Also, chitosan-GLA and chitosan-H₂SO₄ beads showed higher desorption values than chitosan beads in NaOH solutions due to their resistance and mechanical strength on this medium [52].

On the other hand, studies made about the adsorption capacity of RB5 dye into chitosan hydrogels beads crosslinked with glutaraldehyde did not show any significant decrease in the adsorption behavior. The results showed more efficient adsorption values of RB5 at pH values closer to 5-7, with not much difference in the adsorption capacity obtained from crosslinked chitosan beads and non-crosslinked chitosan beads [53].

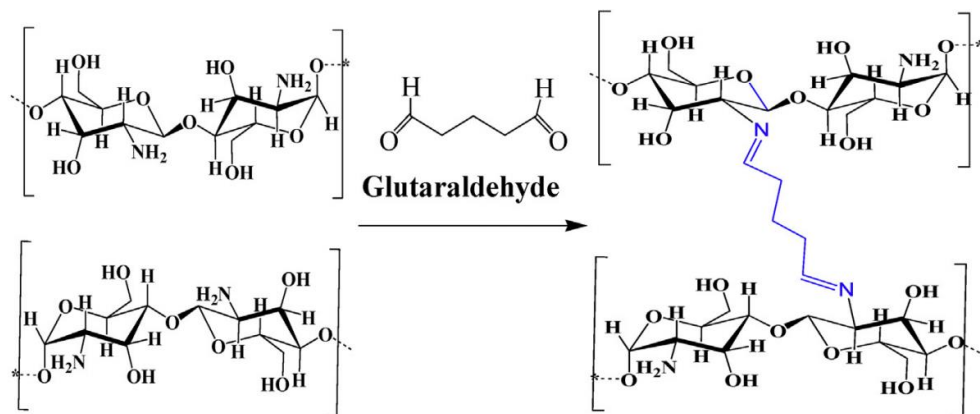


Figure 1. Chemical structure of chitosan chemicaly cross-linked with glutaraldehyde [54].

2.5 Magnetite influence on adsorption and desorption capacities of chitosan hydrogel beads

Magnetic particles have become lately one of the most developed areas in the material science. Properties like its specific surface area, microstructure, and sorption capacity make magnetic gels and aerogels applicable to areas such as biomedicine, medicine, electric and electronic devices, pharmacology, nanotechnology, and used in microfluidic devices, oil sorbents, microsensors for cancer therapy, water treatment, drug delivery, etc. [55-57].

On waste-water treatment, studies on the applicability of magnetic hydrogels have been made. Anastasova et al. describe the pure magnetite gel or ferric gel prepared by direct gelation of magnetite hydrosol under the influence of propylene oxide proton scavenger. The structure of the hydrogels is based on 10 nm of magnetite nanoparticles joined by Fe-O-Fe bonds, with a dark brown viscous appearance. It was possible to describe the adsorption behavior through a Freundlich isotherm, reaching the sorption equilibrium within 24 hours after phase mixing. The material showed higher adsorption capacities for metal ions such as Cr^{6+} and Pb^{2+} with 225% of adsorption capacity, up to 26 mg/g and 53 mg/g, respectively, compared to the unmodified magnetic nanoparticles [58].

Another study published by Paulino, A., Belfiore, L. et al. developed a chitosan-based hydrogel, graft copolymerized with methylenebisacrylamide and poly(acrylic acid), and adsorption kinetics studies onto Pb(II), Cd(II), and Cu(II) were performed. Using the Fickian diffusion model, they concluded that the mass transfer mechanism of water in hydrogels varied when magnetite was present, presenting diffusion and macromolecular structural relaxation mechanisms. The best isotherm models fitted were Langmuir, Freundlich, and Redlich-Peterson, indicating a variation in the physicochemical adsorption phenomena of the hydrogels. Hydrogels and metal ions adsorbed were recovered quickly by applying an external magnetic field [59].

2.6 Adsorption Mechanisms

For understanding the adsorption process between hydrogels adsorbents and adsorbates, some mathematical distributions can be studied to analyze the interaction and predict the equilibrium between liquid and solid phases of the adsorbate molecules at a particular

temperature [60]. The relations are quantified by the adsorbed solid in the solid adsorbate q_{\max} ($\mu\text{mol}/\text{mg}$.) and the equilibrium concentration in solution C ($\mu\text{mol}/\text{dm}^3$). Several isotherms usually used are Henry's isotherms, Langmuir adsorption isotherms, Freundlich Isotherms, Temkin isotherms, and Sips isotherms, resulting in better experimental fitness data compared to others.

2.6.1 Henry's Isotherms.

Henry's isotherm is the simplest isotherm distribution, which fits better at low adsorbate concentrations, assuming that all the adsorbate molecules are separated and isolated from neighbor molecules [61]. The equilibrium adsorbate concentrations are related to the following *Equation 1*:

$$q_e = K_{HE}C_e \quad (1),$$

being q_e the amount (mg/g) of adsorbate at equilibrium, K_{HE} the Henry's adsorption constant and C_e the equilibrium concentration of the adsorbate into the adsorbent.

2.6.2 Langmuir adsorption isotherm.

When the sorption process follows a Langmuir isotherm model, it is assumed monolayer adsorption, where the adsorbent has a homogeneous surface with active sites, and sorbate molecules are subjected to sorption. The nature of the binding sorbate may be physical or chemical, and there is no interaction between the adsorbed molecules in the monolayer [53]. The equilibrium adsorbate concentrations are related into *Equation 2*:

$$q_e = \frac{(K_L q_m C_e)}{(1 + K_L C_e)} \quad (2),$$

where C_e (mg/L) and q_e (mg/g) refer to equilibrium adsorbate concentration and equilibrium amount of adsorbates adsorbed, respectively. K_L refers to Langmuir constant related to adsorption capacity (mg/g), which depends on the adsorbent's area and porosity, and q_m (mg/g) is the maximum adsorption capacity of the adsorbent [62].

Equation 3 is often used to speculate the possible affinity between adsorbate-adsorbent

$$R_L = \frac{1}{1 + bC_0} \quad (3).$$

In this equation b is a Langmuir correlation constant, C_0 is the initial concentration and R_L is a predictor parameter. When $R_L = 0$, the type of isotherm is irreversible, if $R_L = 1$ it means a linear isotherm, if $R_L > 1$ the isotherm adsorption by Langmuir model is unfavorable, and if $0 < R_L < 1$ the isotherm model becomes favorable.

2.6.3 Freundlich adsorption isotherm.

The Freundlich adsorption isotherm is a purely empirical equation indicated for heterogeneous surfaces and considering multilayer adsorption. In this distribution isotherm, the adsorbed molecules are considered less than the number of active sites on the adsorbent and considering only a monolayer formation, enabling the formation of subsequent layers [61]. The distribution fitting of the Freundlich isotherm is expressed as follows in *Equation 4*,

$$q_e = K_F C_e^{\frac{1}{n}} \quad (4).$$

In this expression, K_F represents the adsorption capacity (L/mg) and $\frac{1}{n}$ represents the adsorption intensity, energy distribution, and heterogeneity of the adsorbate sites [61].

2.6.4 Temkin adsorption isotherm

The Temkin adsorption isotherm model consider the interactions between adsorbate-adsorbate and the heat of adsorption (ΔH_{ads}), which varies inversely concerning the increased surface coverage during the adsorption process [63]. The linear expression of Temkin adsorption isotherm is expressed in *Equation 5*:

$$q_e = \frac{RT}{b} \ln K_T + \frac{RT}{b} \ln C_e \quad (5),$$

where b is a constant involving the heat of sorption (J/mol) and K_T belongs to the Temkin isotherm constant [61].

2.6.5 Redlich-Peterson isotherm model

The Redlich-Peterson adsorption isotherm is an empirical equation that relates Langmuir and Freundlich isotherm parameters used to study and fit adsorption equilibrium. It provides

more significant accuracy than the Langmuir and Freundlich isotherm equations. The adsorption mechanism is a mix of both and does not follow ideal monolayer adsorption behavior, and it can be applicable at homogeneous or heterogeneous systems. The Redlich-Peterson expression is defined in *Equation 6*,

$$q_e = \frac{K_{RP}C_e}{1+aC_e^n} \quad (6),$$

where K_{RP} and a are the modified Redlich-Peterson isotherm model constants whose units correspond to $\text{dm}^3 \cdot \text{g}^{-1}$ and $\text{dm}^3 \cdot \text{mg}^{-1}$ respectively, and n is the Redlich-Peterson isotherm exponent [61]. At a high solution concentration of the adsorbate the equation behaves closely to the Freundlich equation. Meanwhile, when n is equal to 1, the equation reduces to the Langmuir equation, where a constant is related to adsorption energy. Finally, when n is equal to 0 the equation becomes Henry's equation.

2.7 Adsorption Kinetic Studies

The evaluation of the adsorption kinetics allows to determine the rate of adsorbate retention or release from the liquid solution to a solid interface at a given amount of adsorbent, temperature, and pH. The type of adsorption can be carried out by two mechanisms that explain the type of adsorbate-adsorbent interaction, which are: physisorption and chemisorption. Physisorption or physical sorption is related to the weak non bonding attraction forces such as van der Waals forces, while chemisorption or chemical sorption electron transfer is involved between adsorbate and adsorbent. For analyzing these mechanisms, kinetic models have been developed and are detailed below.

2.7.1 Pseudo-First-Order Kinetic Model

The pseudo-first-order model describes the interaction adsorbate-adsorbent by the following *Equation 7*

$$\frac{dq_t}{dt} = k_1(q_e - q_t) \quad (7),$$

where k_1 refers to the rate constant of the pseudo-first-order model [s^{-1}] and q_t and q_e are the amount of adsorbate adsorbed onto the adsorbent [mg/g] at time t and the equilibrium, respectively [64].

2.7.2 Pseudo-Second-Order Kinetic Model

The pseudo-second-order kinetics assumes that the available sites on the adsorbent are a determinant parameter in the increase of the rate of adsorption, and the amount of solute in the adsorbent surface has not any influence on the reaction rate [65]. The pseudo-second-order kinetics model can be used to determine initial solute uptakes and the adsorption capacity of the adsorbent [66]. The pseudo-second-order kinetic model is expressed in *Equation 8*,

$$q_t = \frac{t}{\frac{1}{k_2 q_e^2} + \frac{t}{q_e}} \quad (8),$$

where k_2 is de pseudo second order rate constant [$g.mg^{-1}.min^{-1}$], q_t and q_e are the amount of adsorbate adsorbed onto the adsorbent [mg/g] at time t and at the equilibrium, respectively, and t refers to the time [s].

2.7.3 Intraparticle Diffusion Model

The intraparticle diffusion model suggests that the adsorption process involves three steps: (1) film diffusion, in which the mass of solute in solution is transferred to the adsorbent, (2) surface diffusion, and (3) pore diffusion. Surface diffusion and pore diffusion are simultaneous processes, while film diffusion is independent of the other steps [65]. The intraparticle diffusion is studied in *Equation 9*:

$$q_t = k_d t^{\frac{1}{2}} + C \quad (9),$$

where k_d represents the intraparticle diffusion coefficient [$mg.g^{-1}.min^{-1}$], t refers to the time, and C is the intraparticle diffusion constant ($mg.g^{-1}$), which is related to the boundary layer thickness and assumes that the larger is this constant, the greater is the contribution of the surface adsorption on the rate-controlling process [64]. Since this equation has a linear form, the C constant represents the intercept with the y-axis of the graph. If the intercept passes

through the origin, it indicates that the intraparticle diffusion model is the only rate limiting step [64].

2.8 Thermodynamic Adsorption Studies

Thermodynamic adsorption studies allow determining the spontaneity and feasibility for the adsorption process to take place. During adsorption studies, parameters such as the heat of enthalpy (ΔH°), the Gibbs free energy (ΔG°), and entropy (ΔS°) are determined by the equations 10, 11, and 12 respectively:

$$\ln K_d = \frac{\Delta S^\circ}{R} - \frac{\Delta H^\circ}{RT} \quad (10),$$

$$K_d = \frac{q_e}{C_e} \quad (11),$$

$$\Delta G^\circ = \Delta H^\circ - T\Delta S^\circ \quad (12),$$

where K_d corresponds to the thermodynamic equilibrium constant, ΔH° [kJ/mol] is the standard molar sorption enthalpy at temperature T, ΔS° [kJ/mol] is the standard molar sorption entropy, R is the universal gas constant [J/molK], T is absolute temperature [K], q_e is the amount of adsorbate adsorbed onto the adsorbent [mg/g] at the equilibrium sorption, C_e is the equilibrium adsorbate concentration, and ΔG° [kJ/mol] is the standard molar Gibbs free energy.

3 PROBLEM STATEMENT

Environmental problems caused by toxic metal pollutants have become an issue of great concern due to their high toxicity rate, permanence in the environment, and bioaccumulative tendency. Toxic metal contamination comes from natural resources and anthropological resources, mainly industrial and mining activities, the leading cause of the increasing contamination in the aquatic ecosystems, giving rise to environmental problems affecting flora and fauna and causing public health concerns to the humans. Nowadays, several methods have been developed for toxic metal removal from wastewater, such as chemical precipitation, ion exchange, membrane filtration, coagulation-flocculation, flotation, and adsorption. This last one has become the most widely used method in the removal of toxic metals due to its low cost, availability and eco-friendly nature, and easy implementation. Under these aspects, magnetic CS-based hydrogels nanocomposites have been proposed as an eco-friendly alternative applied to the removal of toxic metal from water in wastewater treatments.

4 OBJECTIVES

4.1 General Objective

To study the performance of magnetic CS-based nanocomposite hydrogels in the bioremediation for waste-water

4.2 Specific Objectives

To characterize the magnetic CS-based nanocomposite hydrogels via SEM and TEM techniques, FTIR, XPS studies, and swelling experiments.

To evaluate the removal capacity and efficiency of metal ions from aqueous solutions by sorption kinetics studies, sorption equilibrium studies, and adsorption thermodynamic analysis.

5 METHODOLOGY

5.1 Materials

In the present thesis project, the used magnetic and non-magnetic CS-based hydrogel nanocomposites were previously obtained by the drip method mentioned in the “Chitosan-based hydrogel for waste-water treatment” thesis project [23]. For the magnetic and non-magnetic non-cross-linked hydrogels, CS solution with and without magnetite was dropped separately into NaOH 1M solutions using a syringe needle and stored at room temperature for 24 hours. The formed hydrogels were washed and kept in distilled water[23]. For the magnetic and non-magnetic crosslinked hydrogels, some of the obtained hydrogels beads were submerged on glutaraldehyde (GLA) aqueous solutions at 0.35% and 0.75%. The resulting beads were washed and stored in distilled water[23]. The nomenclature and composition of the chitosan-based hydrogels are described in **Table 2**, where the used code X represents the amount (%) of glutaraldehyde and M, the presence of magnetite nanoparticles [23].

Table 2. *Nomenclature of the CS-based hydrogel nanocomposites used in this work.*

<i>Samples</i>	<i>Preparation Method</i>	<i>%Glutaraldehyde</i>	<i>Magnetite</i>
<i>Q_D</i>	<i>Drip Method</i>	-	<i>x</i>
<i>Q_DX_{0,35}</i>	<i>Drip Method</i>	<i>0,35%</i>	<i>x</i>
<i>Q_DX_{0,75}</i>	<i>Drip Method</i>	<i>0,75%</i>	<i>x</i>
<i>Q_DM</i>	<i>Drip Method</i>	-	✓
<i>Q_DX_{0,35}M</i>	<i>Drip Method</i>	<i>0,35%</i>	✓
<i>Q_DX_{0,75}M</i>	<i>Drip Method</i>	<i>0,75%</i>	✓

For the characterization part of the CS-based hydrogels via SEM, TEM, FTIR, XPS, swelling experiments, and adsorption studies, all the samples mentioned in **Table 2** were used. Hydrochloric acid HCl and sodium hydroxide NaOH solutions at 0.5 M and 1 M, respectively, were used to adjust the pH on swelling and adsorption experiments. Potassium dichromate K₂Cr₂O₄ (99%) was employed for the Chromium (Cr⁶⁺) solutions used in the adsorption studies.

5.2 Experimental Description

5.2.1 Morphological and structural analysis

Scanning Electron Microscopy (SEM) analysis

The morphological analyses of the CS-based hydrogel nanocomposites were evaluated by Scanning Electron Microscopy (SEM). An aliquot of the sample was fixed to an aluminum sample holder using a double layer of carbon tape. If metallization was required, it was performed on the Sputter coating Quorum Q150R ES for 30 seconds, generating a gold coating of approximately 20 nm. These analyses were carried out on the SEM Tescan, Mira 3 equipped with a Schottky field emitter.

Transmission Electron Microscopy (TEM) analysis

Solid CS-based hydrogel nanocomposites samples were dispersed in 60% ethanol in a BRANSON 1510 ultrasonic bath for 30 minutes. Next, approximately 5 μL of the sample was placed on a transmission electron microscope grid (formvar / carbon, 300 mesh), and the solvent was removed with filter paper. The staining was carried out with 1% Phosphotungstic Acid for 1 second, the solvent was removed, and it was observed in TEM FEI, Tecnai G2 Spirit Twin equipped with an Eagle 4k HR camera at 80kV.

5.2.2 Chemical composition analysis

Fourier transform infrared spectroscopy (FTIR)

Fourier transform infrared (FTIR) spectroscopy was employed to determine the chemical structure and assess functional groups present on the surface of CS-based hydrogel nanocomposites. Samples of Q_D, Q_DX_{0.35}, Q_DX_{0.75}, and Q_DX_{0.75}M were analyzed in the wide range of the infrared region between 4000 cm^{-1} to 400 cm^{-1} using a Cary 630 FT-IR Spectrometer with the attenuated total reflectance (ATR) sampling technique.

X-ray Photoelectron Spectroscopy (XPS) analysis

X-ray photoelectron spectroscopy (XPS) analysis was performed on CS-based hydrogels nanomposites for analyzing the electronic structure of elements present on the hydrogels. The samples were placed onto a polymeric-based adhesive tape held by a metallic mesh. X-ray

photoelectron spectroscopy uses a PHI 5000 Probe III Scanning XPS Microprobe from Ulvac phi, inc, and for high-resolution deconvolution was used Gaussian functions using Origin 2019b software.

5.2.3 Swelling capacity studies

The swelling degree of magnetite-chitosan nanocomposites hydrogels was determined by getting the weight after and before the swelling process. Samples of chitosan hydrogels (Q_D), crosslinked chitosan hydrogels ($Q_D X_{0.35}$, $Q_D X_{0.75}$), magnetic chitosan hydrogels ($Q_D M$), and crosslinked magnetic chitosan hydrogels ($Q_D X_{0.35} M$, $Q_D X_{0.75} M$) were submerged on aqueous solutions at different conditions, analyzing the dependence of the contact time, pH and temperature on the swelling degree of the hydrogels.

The submerged hydrogels were extracted at different time intervals onto a filter paper to remove water surface excess in the hydrogel and subsequently weigh the swollen samples. The swelling percentage was calculated by *Equation 13*:

$$E_{sr}(\%) = \frac{(W_s - W_d)}{W_d} * 100 \quad (13),$$

where E_{sr} is related to the water absorption percentage of the hydrogels, and W_d and W_s are the dry and swollen weights of the samples, respectively.

For the contact time dependence experiments, the CS-based nanocomposite hydrogels were submerged in distilled water at standard conditions, pH 7 and 25 °C , and the swollen samples were weighted at several time intervals until the weight of the swollen hydrogels was constant. The immersion time was approximately 140 mins. For the pH dependence experiments, the CS-based nanocomposite hydrogels were immersed into pH solutions of 3, 5, 7, 9, and 11 using 1M HCl and 0.5 M NaOH solutions for the acid and basic adjustments, respectively, during an immersion time of 140 mins and a constant temperature of 25°C. For the temperature dependence experiments, the CS-based nanocomposite hydrogels were immersed in distilled water at 25 °C, 35 °C, and 45 °C, during an immersion time of 140 min. The swollen samples were slightly dried and weighed for the respective swelling degree determinations.

5.2.4 UV-Visible spectroscopy characterization for adsorption analysis

Chromium Adsorption experiments

Several batch experiments were carried out in 50 mL beakers with different Chromium Cr^{6+} aqueous solutions concentrations (100 – 1000 ppm) with pH, temperature, and contact time variations. Cr(VI) ions concentration was determined spectrophotometrically using a digital spectrophotometer Uv/Visible model 4211/50 (220 V) measuring adsorption values at 457 nm as the maximum wavelength obtained from different chromium (Cr^{6+}) solutions. Chromium concentrations in the solution were determined using a properly constructed calibration curve.

pH Dependence

The pH dependence was analyzed over $\text{Q}_\text{D}\text{X}_{0.75}\text{M}$ hydrogels samples at a contact time of 4 hr and using the initial concentration of 300 ppm Cr^{6+} solution. The pH values from 3 to 9 were reached using conveniently 0.5M NaOH or 1M HCl, and adsorption experiments were carried out.

Temperature Dependence

Once the optimal pH adsorption medium was determined, isotherm studies were developed by exposing $\text{Q}_\text{D}\text{X}_{0.35}$, $\text{Q}_\text{D}\text{X}_{0.75}$, and $\text{Q}_\text{D}\text{X}_{0.35}\text{M}$, $\text{Q}_\text{D}\text{X}_{0.75}\text{M}$ samples in Cr^{6+} solutions whose initial concentrations ranged from 100 to 1000 ppm until the equilibrium was reached, in 26 hr approximately. Under the optimal pH conditions the temperature was varied from 20 to 45 °C.

Adsorption kinetic study

For the evaluation of the kinetics of the adsorption process of the CS-based hydrogels the absorbance value at 457 nm was recorded, with which the concentration of chromium in solution was determined, in time intervals of 1 hour. Total time for taking measurements was extended up to 26 hours. Different conditions of temperature were evaluated.

Isotherms of Adsorption study

The adsorption isotherms were obtained by plotting the amount of chromium adsorbed (per mg of adsorbent), denoted by q_e versus the equilibrium concentration of chromium ions in solution, denoted by C_e , at the different temperature values mentioned.

The amount of Cr^{6+} ions adsorbed on the CS-based hydrogels per unit mass of adsorbent was calculated according to *Equation 14*:

$$q_e = \frac{(C_i - C_e) * V}{W} \quad (14),$$

where q_e refers to the amount of Cr^{6+} adsorbed on the CS-based hydrogels expressed with the units $\mu\text{mol/mg}$, where C_i and C_e correspond to the initial and equilibrium concentrations (mg/L) of Cr^{6+} solutions, respectively, while V and W are the volume of solution (mL) and the weight (mg) of the adsorbent, respectively [67].

Different isotherms of adsorption models were tested to understand the mechanism by which the adsorption process is occurring.

6 RESULTS AND DISCUSSION

6.1 Morphological and structural analysis of CS-Based Hydrogel Nanocomposites

6.1.1 Scanning Electron Microscopy (SEM) analysis

CS-based hydrogel nanocomposites prepared by drip method were analyzed by Scanning Electron Microscopy (SEM) to illustrate the effect of the presence of a crosslinker and magnetic species on the morphology of chitosan hydrogels. **Figure 2** shows the SEM micrographs corresponding to a) Q_D, b) Q_DX_{0.35}, c) Q_DX_{0.75}, d) Q_DM, e) Q_DX_{0.35}M, and f) Q_DX_{0.75}M samples at 20 and 100 μm of magnification. The images clearly illustrate a difference in the surface morphology based on the degree of crosslinking and the presence or absence of magnetite in the structure. Figures a, b, and c, depicted in **Figure 2** represent the morphology of non-magnetic chitosan hydrogels with a regular and rough surface and randomly arranged pores. This type of morphology could be due to the degree of deacetylation in certain parts of the chitosan or partially crosslinked parts within the structure [68]. It can also be observed that the pore size decreases as the crosslinking degree increases. Thus, the average pore size diameter presented by the Q_D samples (without crosslinking) is (0.5 ± 0.4) μm, and the average pore size diameter from Q_DX_{0.75} samples is (0.25 ± 0.1) μm. This decrease in pore size is directly related to the presence of glutaraldehyde as a crosslinker forming covalent bonds with amino functional groups from close chitosan chains, forming a more compact structure with a more porous and rough surface morphology [68].

On the other hand, Figures d, e and f, depicted in **Figure 2**, show micrographs of the morphology presented in crosslinked and non-crosslinked chitosan samples with the presence of magnetite. It is possible to establish a difference concerning the morphology of the samples without magnetite since magnetic chitosan hydrogels present a larger pore size with porous microstructures organized in a honeycomb pattern. The pore size diameter presented by the Q_DX_{0.35}M and Q_DX_{0.75}M samples is (13 ± 5) μm approximately for both cases. It can be concluded that the presence of magnetite in chitosan hydrogels helps to maintain an ordered structure, larger pore sizes, with well-defined regular shapes, while the presence of the crosslinkers does not seem to have a significant influence on the pore size.

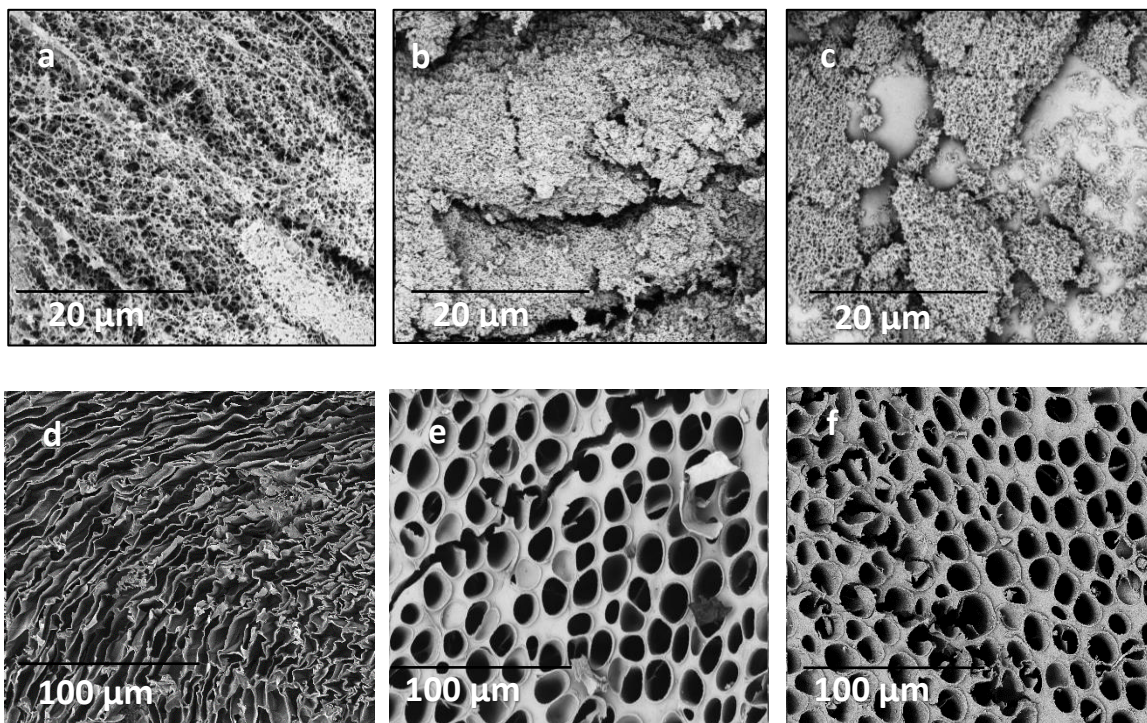


Figure 2. SEM images from samples prepared by drip method a) Q_D , b) $Q_{DX0.35}$, c) $Q_{DX0.75}$, d) Q_{DM} , e) $Q_{DX0.35M}$, f) and $Q_{DX0.75M}$ samples.

Similar results were obtained in SEM analysis presented by Malwal and Gopinath [69] in the synthesis of silica-stabilized chitosan beads for arsenic removal from water. The chitosan beads prepared by the freeze-drying method exhibited high porosity due to lower shrinkage force in their structure [69]. Furthermore, Bin Li et al. suggest that crosslinkers in chitosan beads affect the morphology and size pore, revealing spherical microstructures with a smooth outer organization [68]. On the other hand, analysis on the morphology of polyacrylamide/chitosan/ Fe_3O_4 hydrogels presented a porous network structure with a thin pore wall, with pore sizes about $150\ \mu m$, preserving the porous network structure of the hydrogel. [18].

6.1.2 Transmission Electron Microscopy (TEM) analysis

CS-based hydrogel nanocomposites prepared by drip method also were analyzed by Transmission Electron Microscopy (TEM) to identify the presence of Fe_3O_4 in the hydrogel composition. The TEM images of crosslinked and non-crosslinked chitosan hydrogels are shown in **Figure 3** (a-c). A regular and semi uniform surface is observed in the single pure chitosan and an increase of crosslinker causes agglomerations or clusters in the structure.

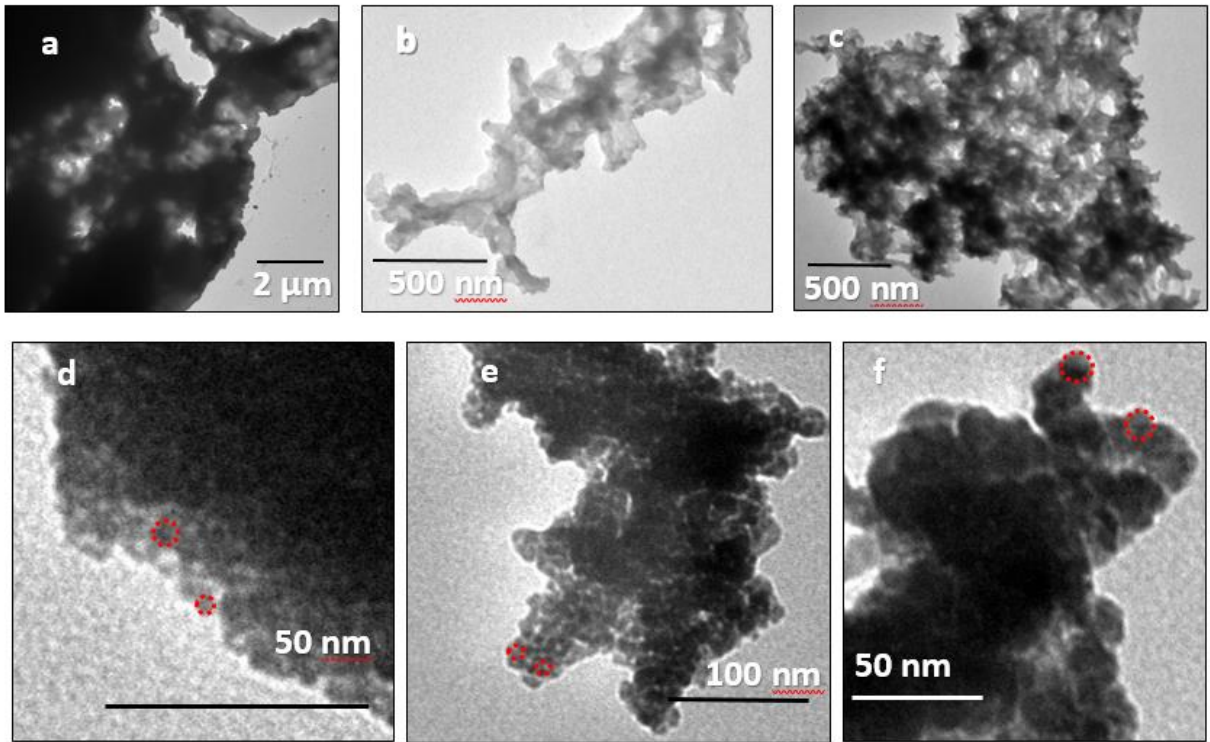


Figure 3. TEM images from samples prepared by drip method a) Q_D , b) $Q_D X_{0.35}$, c) $Q_D X_{0.75}$, d) $Q_D M$, e) $Q_D X_{0.35} M$, f) and $Q_D X_{0.75} M$ samples.

On the other hand, **Figure 3** (d-f) shows crosslinked and non-crosslinked chitosan hydrogels containing magnetite. Dark zones are observed to have spherical shapes of Fe_3O_4 nanoparticles uniformly incorporated in a chitosan matrix (lighter gray zones). Confirming the results obtained by SEM images, the presence of magnetic nanoparticles in the chitosan polymer causes a well-ordered structure, forming spherical microcapsules inside the matrix. The crosslinking presence seems to impact the size diameter of the spherical nanoparticles by increasing it. The average nanoparticle diameter sizes of the spheres from $Q_D M$, $Q_D X_{0.35} M$, and $Q_D X_{0.75} M$ are $(3 \pm 0.5) nm$, $(11 \pm 0.5) nm$, and $(11 \pm 0.9) nm$, respectively. This could be attributed to the possible cluster formation in the chitosan matrix generated by the crosslinking agent. However there is not significant difference as the crosslinking percentage increases since the size of spheres for $Q_D X_{0.35} M$, and $Q_D X_{0.75} M$ samples is quite similar.

Similar results were found on TEM analysis of crosslinked chitosan montmorillonite composites by Gierszewska et al., where the dispersion of nanofiller in crosslinked matrix and intercalation of chitosan chains is hindered by the covalent crosslinks, which cause a

lower chitosan chain mobility [70]. However, the incorporation of magnetic nanoparticles is shown as well-ordered crystals of composite microcapsules in which the magnetic nanoparticles are embedded in the chitosan matrix in the form of magnetic microspheres of relatively smooth texture [71,72,18].

6.2 Chemical composition studies of CS-based hydrogel nanocomposites

6.2.1 X-Ray Photoelectron Spectroscopy (XPS) analysis

XPS spectra analysis was used to determine the surface chemical compositions of CS-based hydrogel nanocomposites, suggesting possible adsorption sites belonging to chitosan and magnetite in the composites. The evaluated XPS spectra expose the survey spectra of the CS-based hydrogel nanocomposites samples and magnifications in specific regions to evaluate the presence of carbon, oxygen, nitrogen, and iron in the sample.

The survey XPS spectra of the Q_D, Q_DX_{0.35}M, and Q_DX_{0.75}M as representative samples are depicted in **Figure 4**. It is possible to observe three peaks in all samples at approximately 532 e.V, 398 e.V, and 285 e.V corresponding to O1s, N1s, and C1s binding energies. However, there are two peaks at 710 e.V and 724 e.V corresponding to Fe2p binding energies present on Q_DX_{0.35}M and Q_DX_{0.75}M samples but not in Q_D, samples which mean that the magnetic nanoparticles have been successfully embedded in the surface of the hydrogel.

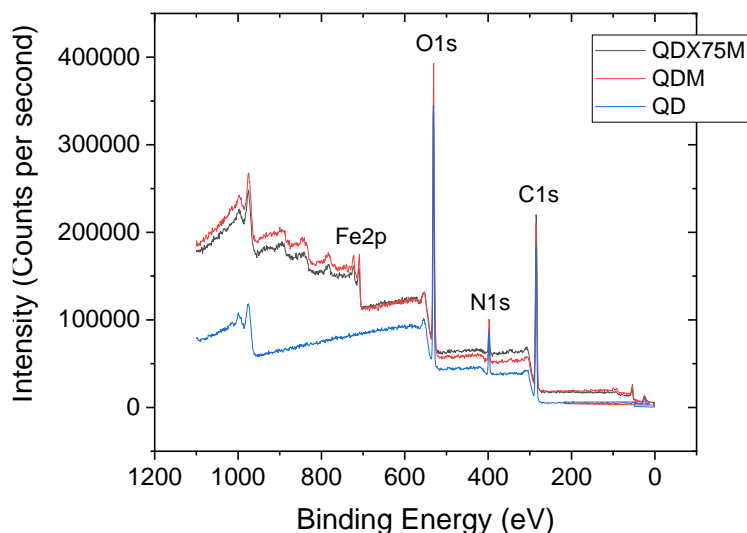
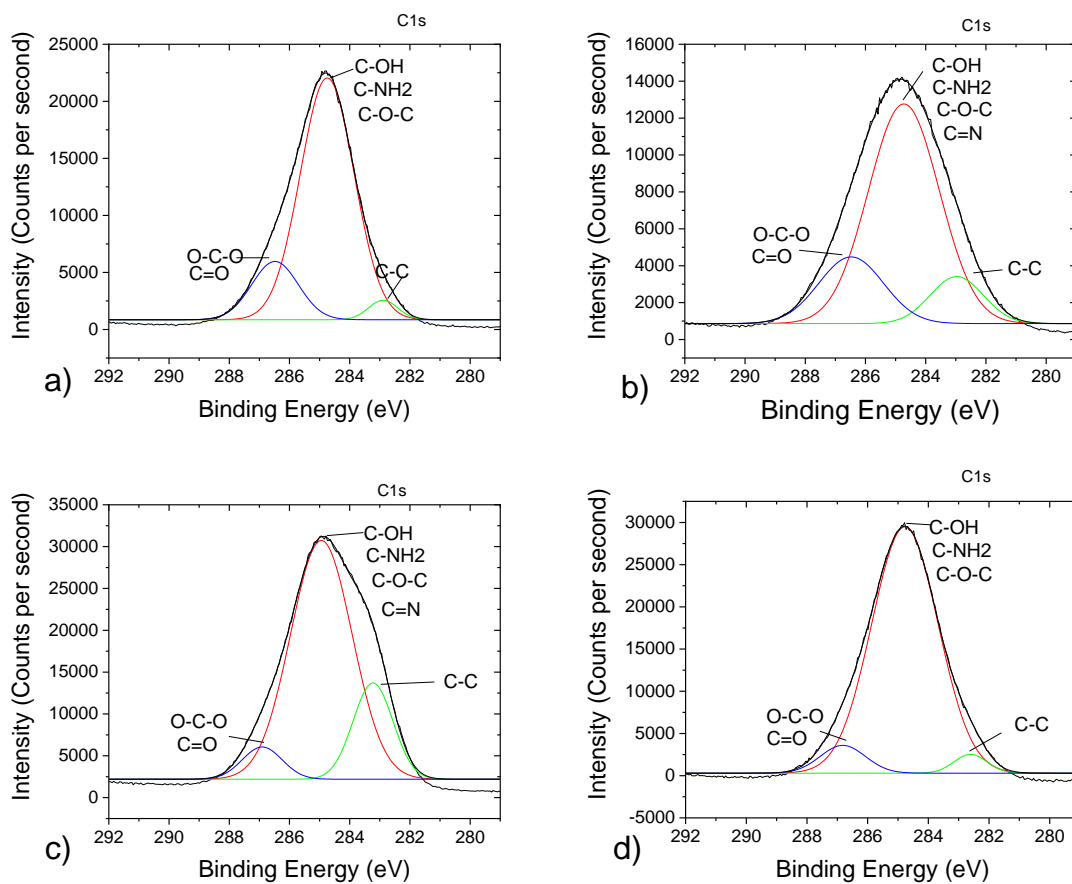


Figure 4. XPS spectra of the survey XPS spectra from Q_D , Q_{DM} , $Q_{DX_{0.75}M}$ sample.

Figure 5 shows the deconvolution for the C1s peaks into gaussian functions of a) Q_D , b) $Q_{DX_{0.35}}$, c) $Q_{DX_{0.75}}$, d) Q_{DM} , e) $Q_{DX_{0.35}M}$, and f) $Q_{DX_{0.75}M}$ samples. The first one, centered at 282.9 e.V, corresponds to the C-C chemical binding, another at 284.8 e.V belonging to C-OH, C-NH₂, or C-O-C chemical binding occurring in the chitosan and crosslinked chitosan structure and another at 286.8 e.V corresponding to O-C-O and possible C=O chemical bindings. According to the database consulted, these results yield values close to those reported by Yap et al. and Ratner and Caster [73- 75]. The results show an increased intensity in the peaks corresponding to C-C bindings as the cross-linking degree increases. This may be due to the addition of alkyl groups induced by the presence of aliphatic carbons from glutaraldehyde in the chitosan structure. Finally, magnetic nanoparticles seem to not present significant changes in the C1s spectra.



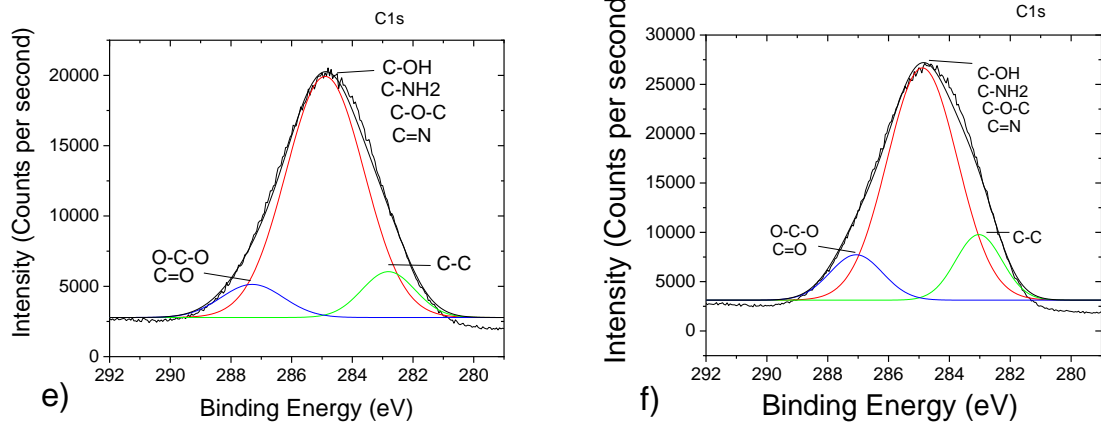
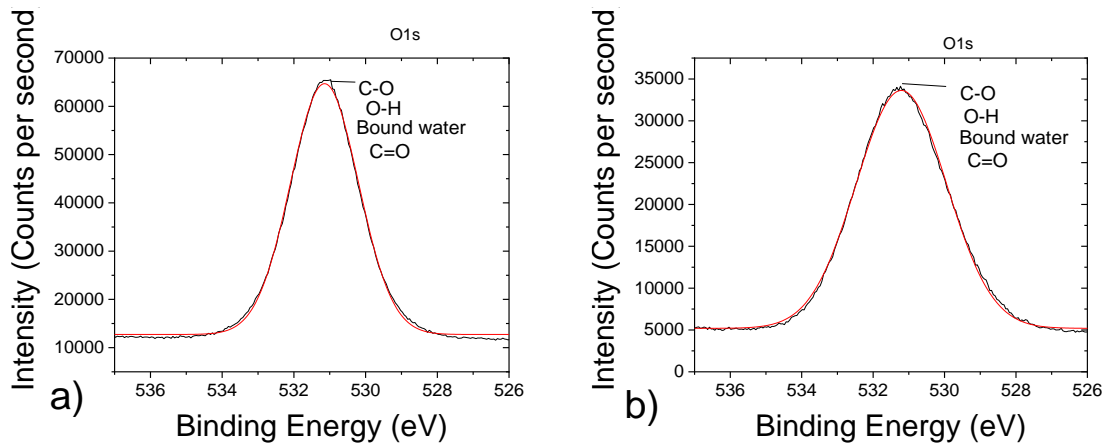


Figure 5. XPS spectra of C1s from a) Q_D , b) $Q_{DX0.35}$, c) $Q_{DX0.75}$, d) Q_{DM} , e) $Q_{DX0.35M}$, and f) $Q_{DX0.75M}$ samples.

On the other hand, **Figure 6** depicts the deconvolution for the O1s spectra for a) Q_D , b) $Q_{DX0.35}$, c) $Q_{DX0.75}$, d) Q_{DM} , e) $Q_{DX0.35M}$, and f) $Q_{DX0.75M}$ samples, showing a deconvolution centered 531.2 eV corresponding to C-O, O-H, bound water, and possible C=O binding interactions. Since there is no modification in the O1s peaks with increasing cross-linker, it can be said that there is no interaction between the crosslinker and the oxygen atoms in the hydrogel structure. However, in **Figures 6** (d-f), a new peak is observed at 528.5 eV belonging to magnetic nanoparticles in Fe-O and Fe-OH chemical bindings [76]. These peaks related to oxygen hydroxyl groups and iron atoms can be explained by or possible interactions between adsorbed water into magnetite surface and chitosan hydroxyl groups [76].



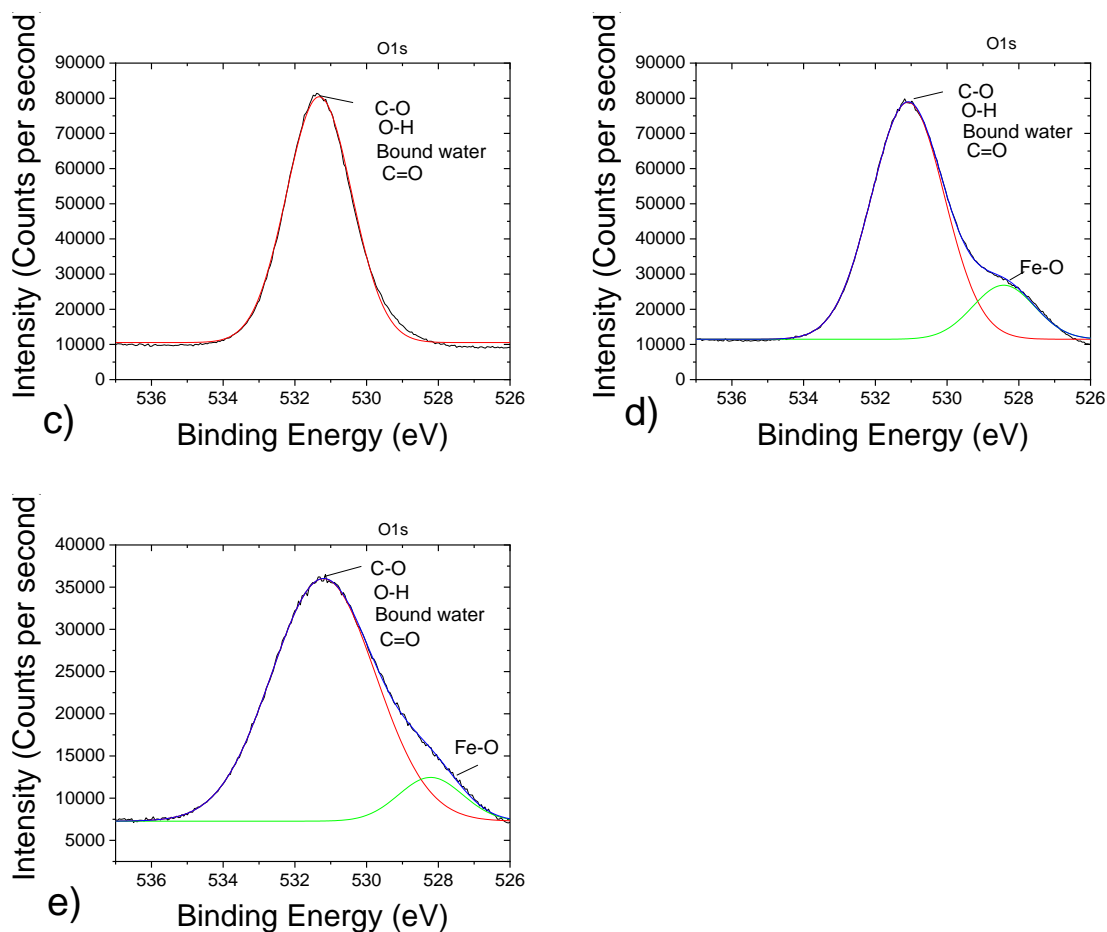


Figure 6. XPS spectra of O1s from a) Q_D , b) $Q_{DX0.35}$, c) $Q_{DX0.75}$, d) Q_{DM} , e) $Q_{DX0.35M}$, and f) $Q_{DX0.75M}$ samples.

For the N1s spectrum depicted in **Figure 7**, a peak at 397, 9 eV in all the samples, corresponding to C-N and free NH_2 chemical bindings, can be seen. From **Figure 7**, it can be observed a tiny peak at 400,7 eV corresponding to possible amino groups in the form of ammonium ions (NH_3^+) [77]. On the other hand, **Figure 7** (b-c) shows an increased peak at 400 e.V as the cross-linking degree increases. This peak corresponds to C=N bindings formed between crosslinker and amino groups from chitosan in cross-linked hydrogels [78]. In the presence of magnetic nanoparticles, as is shown in **Figure 7** (d-f), a more intense peak at 399.6 corresponding to NH_2 -Fe and some C=N chemical bindings, in the case of cross-linked samples, showing some amino groups chelated with iron ions, confirming the presence of magnetic nanoparticles in the structure [76]. Finally, there is an evident decreasing peak on the C-NH₂ peaks while the increasing cross-linking degree, especially on magnetic samples.

This can be explained because some C-NH₂ bonds turn into C=N bonds product of the glutaraldehyde grafting by the crosslinking process.

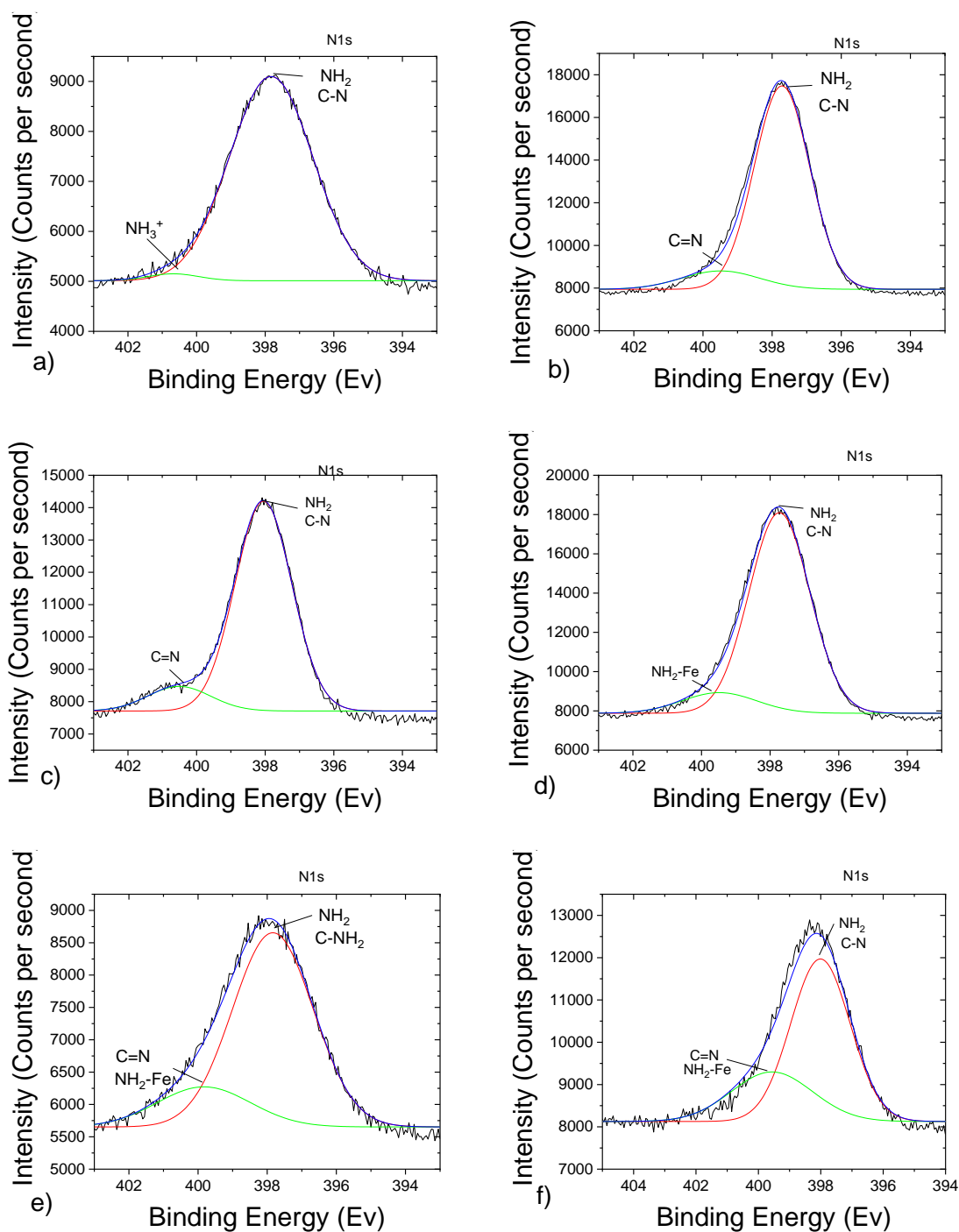


Figure 7. XPS spectra of N1s from a) Q_D, b) Q_DX_{0.35}, c) Q_DX_{0.75}, d) Q_DM, e) Q_DX_{0.35}M, and f) Q_DX_{0.75}M sample.

The peaks corresponding to Fe 2p_{1/2} and Fe_{3/2} binding energies are depicted in **Figure 8.**, whose binding energies are 110.9 e.V and 124.0 e.V, respectively, which is a characteristic pattern for Fe₃O₄ broaden peaks and which are presented only on hydrogels with magnetite. [79]. Wang et al. suggest that the atomic fraction associated with hydrogen bonds, such as hydroxyl groups, increases in samples containing iron, concluding that some nitrogen and oxygen atoms, from hydrogen bondings, take part also in the complex formation of iron-chitosan [76, 80].

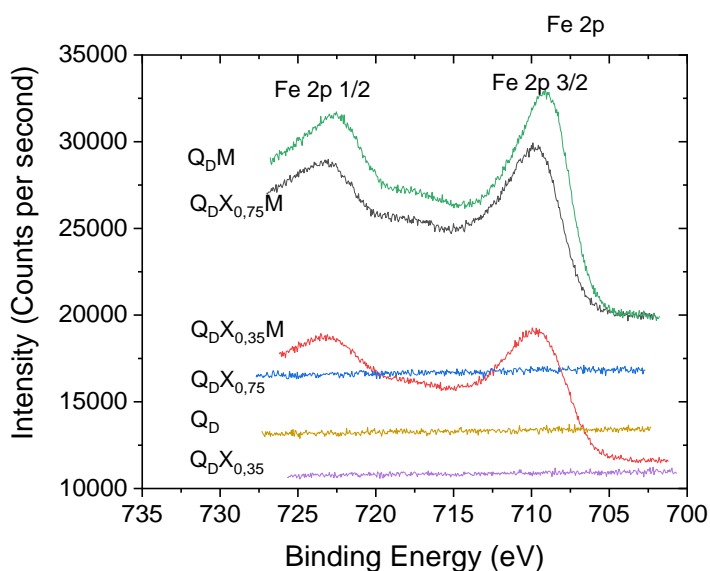
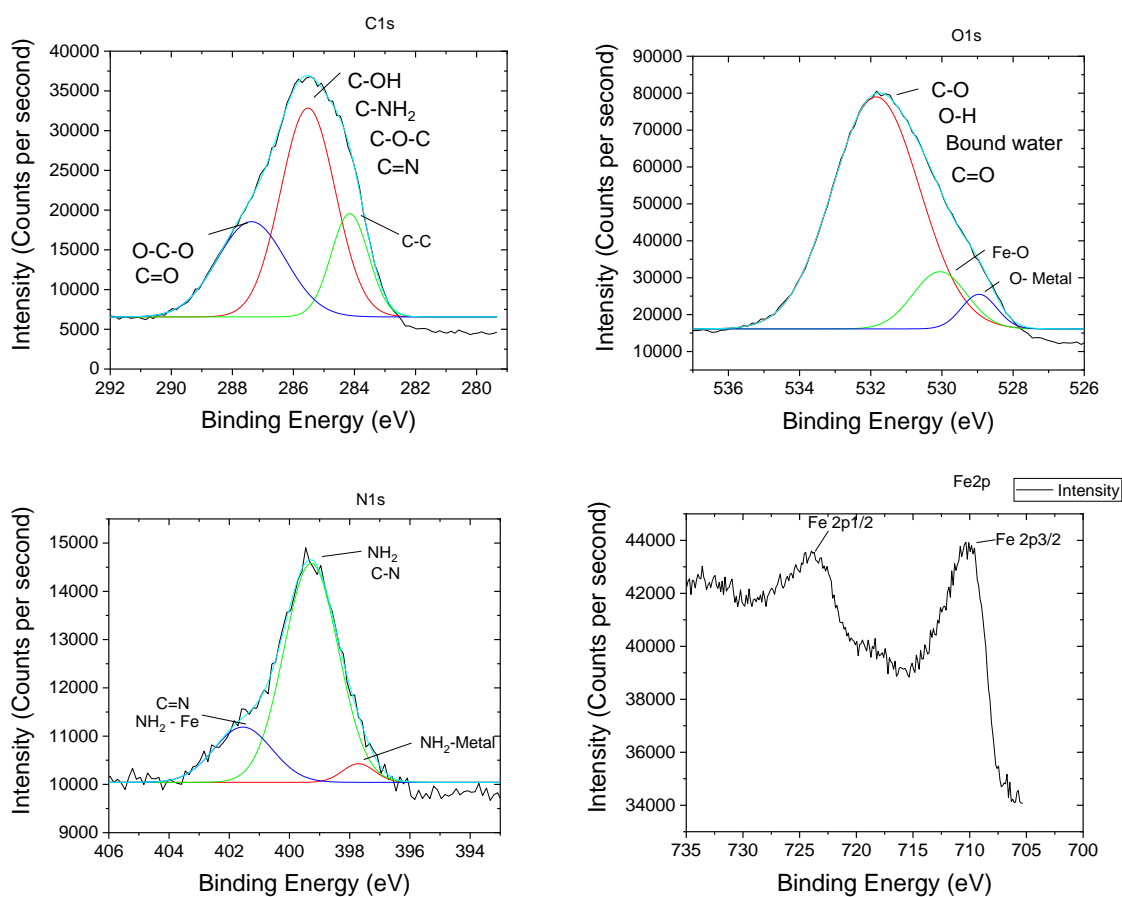


Figure 8. XPS spectra of Fe 2p from a) Q_D, b) Q_DX_{0.35}, c) Q_DX_{0.75}, d) Q_DM, e) Q_DX_{0.35}M, and f) Q_DX_{0.75}M sample.

After the chromium adsorption, the XPS spectrum was obtained for Q_DX_{0.75}M sample. **Figure 9 a)** depicts the C1s region of the sample after chromium adsorption. It is possible to observe a change in the 284.8 e.V belonging to C-OH, C-NH₂, or C-O-C chemical bindings, which can be related to the imino or hydroxyl groups that take part in the Chromium adsorption process [81]. **Figure 9 b)** shows the O1s spectra assigned to the peaks related to O1s photoemissions. A new peak is observed at 528.5 eV relative to the XPS of the sample before chromium adsorption, corresponding to the given interaction between oxygen and Cr atoms arising during the adsorption process [82].

In the same way, **Figure 9 c)** shows the spectra of the N1s region after the adsorption process, with the same two peaks obtained in the XPS before adsorption. However, a new peak located

at 397.7 eV confirms the interaction between the N- Cr atoms [82]. On the other hand, **Figure 9 d**), corresponding to the Fe2p spectrum after adsorption, does not show significant changes concerning the spectrum analyzed before adsorption. Finally, the spectrum of the Cr2p region can be observed in **Figure 9 e**) with two regions corresponding to Cr 2p_{1/2} and Cr 2p_{3/2}. In them, the peaks found at 587.1 eV and 577.4 eV correspond to the Cr(VI) binding energies, and the peaks found at 585.4 and 575, 9 corresponding to the Cr(III) binding energies [74,82]. The results show that both Cr(VI) and Cr(III) coexist adsorbed on the sample surface, thus concluding that chitosan hydrogels not only act in the removal of Cr(VI) in contaminated solutions but also allow Cr(VI) to be reduced into less toxic ions such as Cr(III) [74].



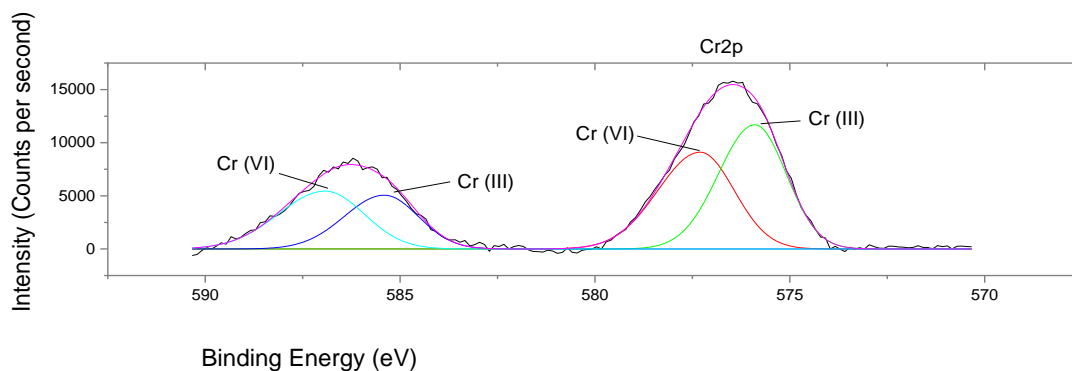


Figure 9. XPS spectra of $Q_{D}X_{0.75}M$ sample after Cr (VI) adsorption for a) C1s, b)O1s, c) N1s, d)Fe2p, and f) Cr2p.

6.2.2 Fourier-Transform Infrared Spectroscopy (FTIR) analysis

Fourier Transform Infrared Spectroscopy (FTIR) analyses were performed for studying the chemical structure of CS-based hydrogel nanocomposites and magnetic CS-based hydrogel nanocomposites, determining the functional groups present on their surface. The Q_{D} , $Q_{D}X_{0.35}$, $Q_{D}X_{0.75}$, and $Q_{D}X_{0.75}M$ samples spectra are shown in **Figure 10**. The broad spectrum band between 3400 cm^{-1} and 3200 cm^{-1} can be assigned to O-H from chitosan and adsorbed water and remaining N-H groups from the chitosan backbone. This band has been slightly broadened in the $Q_{D}X_{0.75}M$ sample compared to the other samples, which can be attributed to some type of interaction between magnetite, amines, and hydroxyl groups from chitosan. The band at 2937 cm^{-1} and 2868 cm^{-1} corresponds to stretching vibrations of aliphatic C-H bonds in the hydrogel structure. These peaks increase their intensity as the GLA cross-linker percentage increases; this can be explained because new alkyl groups from the GLA are incorporated into the hydrogel chitosan backbone [83]. The band near 1656 cm^{-1} is more intense in samples presenting crosslinking. This band is referred to as the C=N imine group formed during the crosslinking reaction from chitosan with GLA, confirming the interaction between free amine groups belonging to chitosan with aldehyde groups from GLA forming a stable imine by the Schiff base reaction [84].

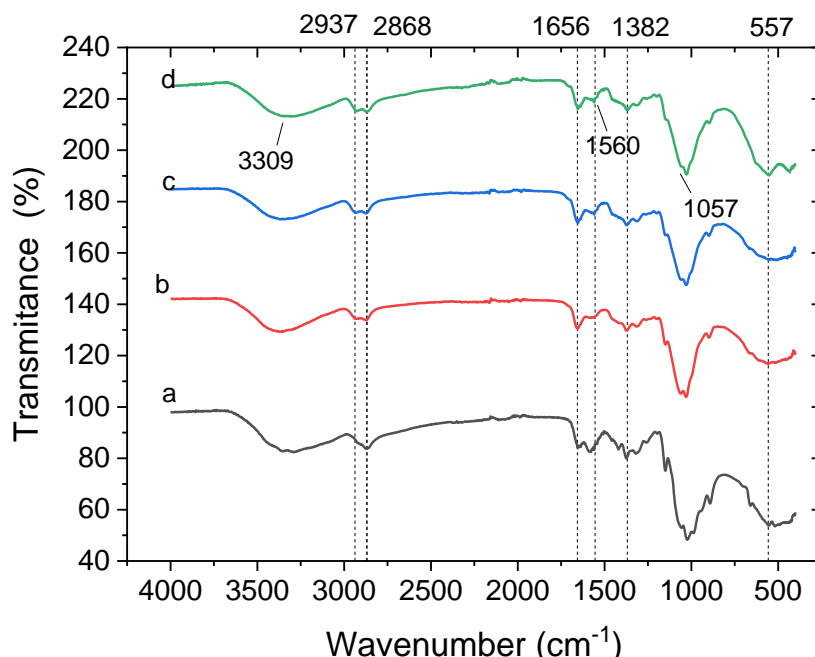


Figure 10. FTIR spectra of the CS-based hydrogel nanocomposites for a) Q_D , b) $Q_{DX0.35}$, c) $Q_{DX0.75}$, and d) $Q_{DX0.75M}$ samples.

The band presented at 1560 cm^{-1} belongs to primary amines NH_2 , which decreases its intensity as the crosslinking degree increases, as the result of some primary amino groups from chitosan turns into imine groups product of the glutaraldehyde grafting. The band at 1382 cm^{-1} corresponds to deformation vibrations of N-H in primary amines and at 1057 cm^{-1} refers to C-O in C-OH stretching vibration. Finally, the strong band near 560 cm^{-1} exhibits the stretching vibration of the Fe-O group, corresponding to the magnetite phase present in the crosslinked chitosan nanocomposite structure [85]. All these stretching band vibrations reaffirm the results obtained in the XPS analysis and confirm that the grafting with glutaraldehyde and magnetic nanoparticles has been taken place in the chitosan hydrogel structure.

6.3 Swelling analysis of CS-based hydrogel nanocomposites.

Swelling experiments of CS-based hydrogel nanocomposites synthesized by the drip method (Q_D , $Q_{DX0.35}$, $Q_{DX0.75}$, Q_{DM} , $Q_{DX0.35M}$, and $Q_{DX0.75M}$ samples) were carried out in distilled water (pH ~ 7) and at $20\text{ }^\circ\text{C}$ for approximately two and a half hours. The swelling degree for each sample was obtained by the change in weight observed, attributed to the

content of water absorbed. *Equation 13* was used for that determination. **Figure 11** shows the swelling kinetics and time-dependent behavior of the CS-based hydrogel nanocomposites. The samples exhibited a rapid increase in water content, reaching the equilibrium near to 60 min. Non-crosslinked hydrogels (Q_D, Q_{DM}) showed a higher swelling percentage than that for crosslinked chitosan and magnetic crosslinked chitosan hydrogels. The swelling percentage decreases as the amount of crosslinking in hydrogels increases indicating that crosslinking degree reduces structure flexibility, decreasing the free volume inside the networks and affecting the amount of water absorbed in the chitosan hydrogel [86]. Furthermore, the FTIR and XPS results showed the formation of imine groups C=N in the hydrogel attributed to the grafted GLA in the chitosan backbone, the stretching vibrations and binding energies related to C-NH₂ chemical bonds decrease; as a consequence, there are fewer amino groups available for hydrogen bonds and therefore, less swelling capacity on the hydrogels.

On the other hand, magnetic chitosan hydrogels presented a lower swelling degree than magnetite-free chitosan hydrogels. Magnetic nanoparticles occupy some of the available pores in the hydrogel, reducing water diffusion, developing a more compact structure, and decreasing the swelling capacity. Although SEM images showed that magnetic crosslinked chitosan hydrogels showed a well-defined porous structure with larger pore size, FTIR and XPS analysis confirm that some amino and hydroxyl groups are chelated with iron ions the complex formation of iron-chitosan. Therefore, the available amino and hydroxyl groups for hydrogen bindings decrease, decreasing the swelling degree [76, 87].

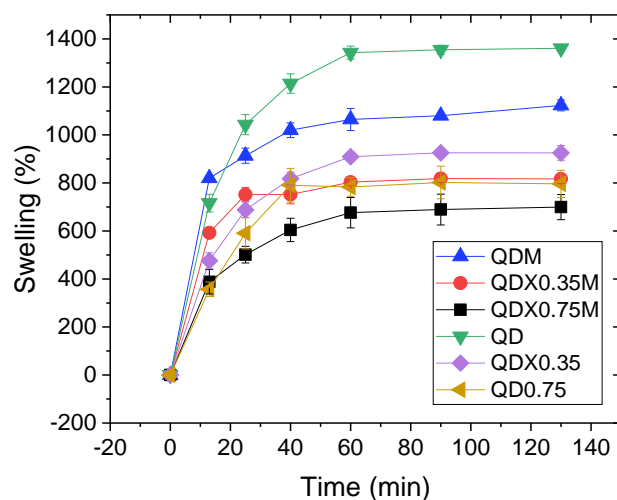


Figure 11. Swelling kinetics of chitosan hydrogels at pH 7 for Q_D , $Q_{DX0.35}$, $Q_{DX0.75}$, Q_{DM} , $Q_{DX0.35M}$, and $Q_{DX0.75M}$ samples, at room temperature.

The response of the CS-based hydrogel nanocomposites to different aqueous swelling conditions is presented in **Figure 12**. For this characterization, the different CS-based hydrogel nanocomposites were submerged on aqueous solutions of pH 3, 5, 7, 9, and 11 for about 60 min at room temperature of 20 °C, and the swelling degree was obtained at the equilibrium. For the non-crosslinked (Q_D and Q_{DM}) samples, the acid pH swelling experiments were not possible because non-crosslinked chitosan hydrogels dissolved easily in an acid medium because of the protonation of their hydroxyl and amine groups which makes chitosan soluble in water.

CS-based hydrogel nanocomposites reveal a slight increase in swelling when exposed to acidic and basic conditions. This behavior can be explained by the positively charged surface of chitosan generated by ($-NH_3^+$) groups when they are exposed to an acid medium, and the deprotonation of the residual amino groups ($-NH_2$) into ($-NH^-$) formation in a basic medium. The effect of the same charges causes long intermolecular distances because of the electrical repulsion. Similar behavior was reported by Jeong S. et al. in the swelling characterizations of chitosan and polyacrylonitrile semi-interpenetrating network (semi-IPNs) hydrogels. The semi-IPNs swelled lower than pH 2 and higher than pH 10 values and shrunk at pH 7. In acid and basic solutions, hydrogels with higher chitosan content resulted

in increased swelling behavior for the internal ion osmotic pressure generated by the charge repulsion of the protonated and deprotonated amino groups, respectively [88].

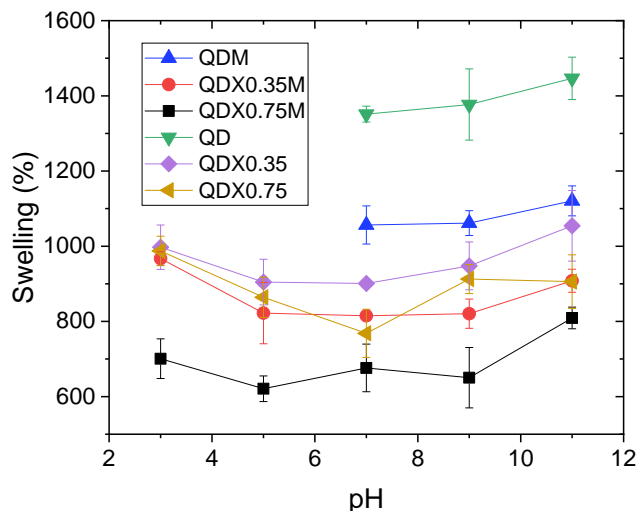


Figure 12. *pH-dependency swelling of Q_D , $Q_{DX0.35}$, $Q_{DX0.75}$, Q_{DM} , $Q_{DX0.35M}$, and $Q_{DX0.75M}$ samples at room temperature.*

Finally, the response of crosslinked CS-based magnetic nanocomposites hydrogels to different temperatures was evaluated, and the results are presented in **Figure 13**. The different hydrogels were exposed to an aqueous medium at pH 7, reaching the swelling equilibrium in about 60 min, exposed to 20 °C, 35 °C, and 45 °C. All the hydrogels samples present a slight increase in swelling as the temperature rises from 20 °C to 45 °C. Non-crosslinked hydrogels swelled the most with the increase of temperature compared to the others. Higher temperatures result in relaxation of the hydrogel chains and dissociation of intramolecular interactions such as hydrogen bonding between the same chains of the polymer. Crosslinking hydrogels did not result in significant swelling because the tighter structures prevented the free movement of the chains and, therefore, less water swelling capacity.

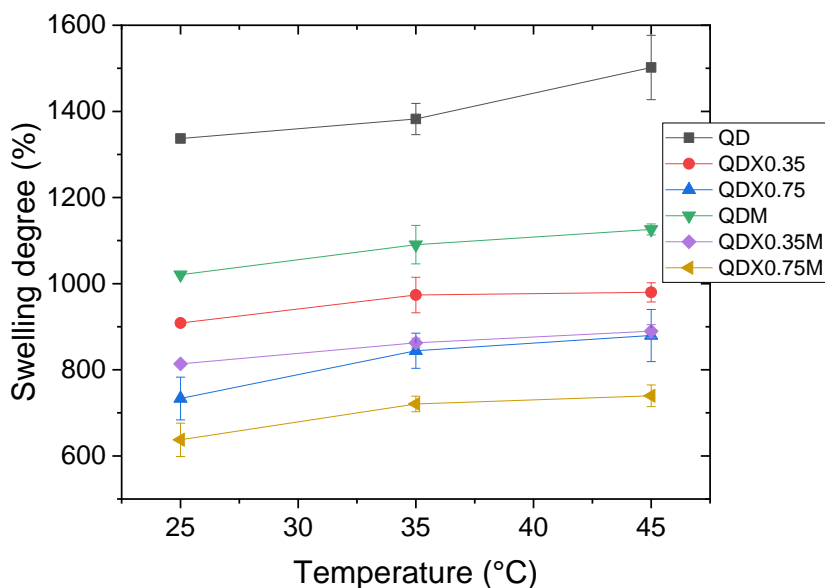


Figure 13. Temperature dependency swelling of Q_D , $Q_{DX0.35}$, $Q_{DX0.75}$, Q_{DM} , $Q_{DX0.35M}$, and $Q_{DX0.75M}$ s at pH 7.

Ghaemy and Naseri derived similar temperature dependence on swelling chitosan nanohydrogel networks synthesized with glyceroldiglycidylether (GDE) and poly(dimethylsiloxane) (PDMS) as crosslinkers. The increase in temperature proportionally affected the nanohydrogels' swelling, resulting in more significant swelling to non-crosslinked hydrogels. They concluded an expansion in the nanohydrogel networks and some associations and dissociations of hydrogen bonds between functional groups inside the hydrogels induced by increased temperature [89].

6.4 Adsorption Analysis

6.4.1 Adsorption of Chromium (Cr^{6+}) on CS-based hydrogel nanocomposites

Effect of the initial concentrations.

Several Cr^{6+} sorption experiments were developed using 5 mL of $K_2Cr_2O_7$ solutions at 100, 150, 200, 250, 300, and 400 ppm concentrations and approximately 4.5 mg of magnetic and non-magnetic chitosan hydrogels for $Q_{DX0.35}$, $Q_{DX0.75}$, $Q_{DX0.35M}$, and $Q_{DX0.75M}$ samples. The conditions under which these analyzes were developed are at 25 °C, and equilibrium

time of 25 hours. The results are shown in **Figure 14**, where the amount of Cr^{6+} adsorbed obtained from *Equation 14*, expressed in $\mu\text{mol}/\text{mg}$ is plotted against Cr^{6+} initial metal composition expressed in ppm.

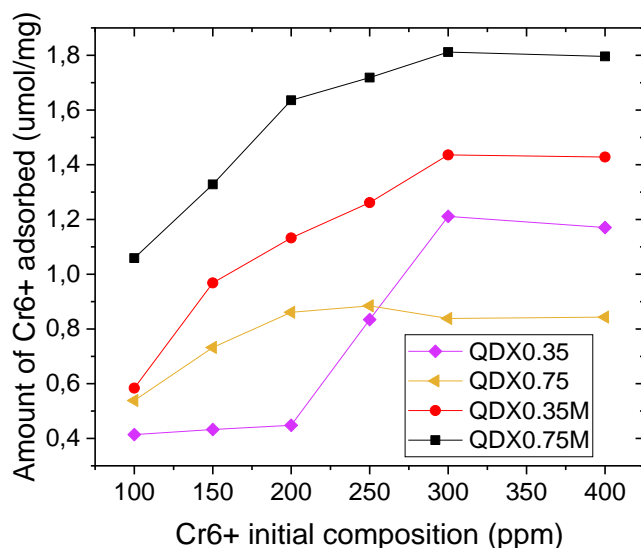


Figure 14. Effect of initial concentration on the Cr^{6+} adsorption experiments on $Q_{DX0.35}$, $Q_{DX0.75}$, $Q_{DX0.35M}$, and $Q_{DX0.75M}$ samples at 25°C and 25 hours of exposure.

The results show a good performance for $Q_{DX0.75M}$ hydrogels over the other types. Since the results obtained in the SEM analysis showed that the pore size diameter increases significantly in magnetic crosslinked hydrogels compared to non-magnetic hydrogels, increasing the adsorption surface area. On the other hand, $Q_{DX0.35}$ sample presents higher adsorption than $Q_{DX0.75}$ sample because when the crosslinking degree increases, the available amino groups for adsorption decrease due to the formation of imine groups confirmed on the XPS and FTIR analyses.

Figure 14 also exhibits an increase in the Cr^{6+} uptake when the Cr^{6+} solution concentrations increase from 100 to 300 ppm, reaching their maximum at 300 ppm with the adsorption quantity (q) of $1.8117 \mu\text{mol}/\text{mg}$., and then, the “ q ” values tend to decrease slightly. This behavior can be explained because when metal ion concentration increases, the probability of interactions between metal ions and the adsorbent also increases, reaching a saturation point, in this case at 300ppm [90]. Therefore, the $Q_{DX0.75M}$ sample and 300 ppm,

as the most efficient sample and initial concentration in the adsorption of chromium Cr^{6+} , were applied to the subsequent adsorption tests.

Effect of adsorbate-adsorbent ratio.

Cr^{6+} sorption experiments were conducted with $\text{QDX}_{0.75}\text{M}$ samples in solutions of 300 ppm Cr^{6+} concentration at 25 °C, pH 7, and 24 hours of exposure. The relation solution volume [mL] - hydrogel weight [mg] was varied (from 1:1, 2:1, and 3:1), and the amount of Cr^{6+} adsorbed was reported, as shown in **Table 3**. Cr^{6+} removal was higher at 1:1 ratio decreasing while the solution volume increased. It can be concluded that although the volume of the solution increases, if the amount of hydrogel is constant, the number of adsorption sites will remain constant; therefore, the metal adsorption does not increase when the volume of the metal solution increases. Therefore, a relation of 1:1 solution volume-hydrogel weight [mL/mg] was selected for the next experiments.

Table 3. “q” values obtained from different Solution volume: Hydrogel weight ratios of the $\text{QDX}_{0.75}\text{M}$ sample in the adsorption of Cr^{6+} .

<i>Solution volume: Hydrogel weight ratio [mL/mg]</i>	<i>q [$\mu\text{mol} / \text{mg}$]</i>
1:1	1.8117
2:1	0.81
3:1	0.777

Effect of the initial pH conditions.

Adsorption experiments varying the pH medium were developed on systems solution-hydrogel ratio of 1:1 [mL/mg] at 300 ppm Cr^{6+} concentration and 25 °C, during 24 hours of exposure of the hydrogel, and using 0.5 M of HCl and 1M NaOH for reaching 3 and 11 pH values respectively. The results are presented in **Table 4**. A decrease in the Cr^{6+} removal can be seen while the pH increases, especially at basic conditions. In Cr^{6+} solutions, chromium is founded as HCrO_4^- and $\text{Cr}_2\text{O}_7^{2-}$ ions [91], at acid conditions, amino groups from the magnetic crosslinked-chitosan hydrogel are protonated being positively charged and generating an electrostatic attraction to the negative anions (HCrO_4^- and $\text{Cr}_2\text{O}_7^{2-}$) [67].

Table 4. “q” values obtained from different pH solution in the adsorption of Cr⁶⁺ by Q_DX_{0.75}M sample at room temperature:

<i>pH Solution</i>	<i>q [μmol /mg]</i>
3	2.1323
7	1.6578
11	0.9361

Contrarily, at basic conditions, many hydroxyl and amino groups from chitosan in the hydrogel are deprotonated, getting negatively charged, and therefore, generating repulsive forces between the magnetic crosslinked-chitosan hydrogel and chromate ions, decreasing its adsorption. It can be concluded that chromium adsorption depends on the pH conditions. Chromium uptake increases when pH values decrease. For avoiding the possible dissolution of Fe₃O₄ from the magnetic hydrogels on an acid medium, the adsorption experiments on this project were performed at neutral solutions.

Effect of temperature and contact time.

For analyzing the effect of the temperature and contact time, three Q_DX_{0.75}M samples were submerged on Cr⁶⁺ solutions of 300 ppm at 1:1 solution-hydrogel [mL/mg] ratio. The experiments were conducted at pH 7, at 25 °C, 35 °C, and 45 °C, for approximately 25 hours and measuring the amount of Cr⁶⁺ adsorbed “q” in several time intervals. As is shown in **Figure 15**, there is an increase in the Cr⁶⁺ removal when the contact time increases until reaching the equilibrium (nearly 23 hours). After 23 hours, the metal ion uptake was slower than the rapid metal ion uptake before reaching equilibrium.

Figure 15 also reveals a dependency of the adsorption quantity of chromium with the temperature. The adsorption capacity of Q_DX_{0.75}M gradually increases as the temperature is increased from 25°C to 45°C. The maximum adsorption quantity values at equilibrium “q_e” were 1.6478, 1.9834, and 2.7074 for 25 °C, 35 °C, and 45 °C, respectively, concluding that the increase in temperature enhances the adsorption process.

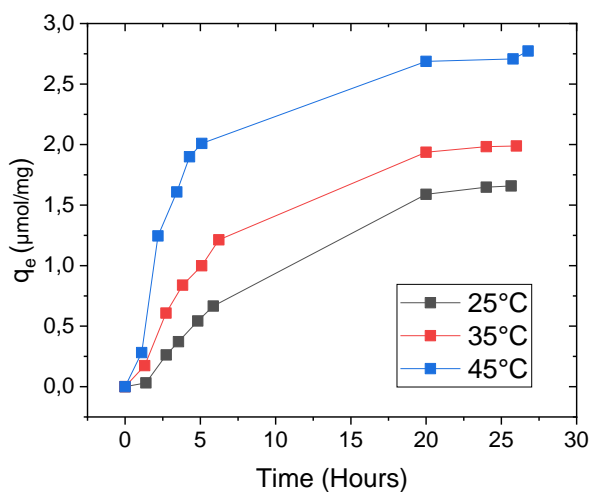


Figure 15. Effect of temperature and contact time on $Q_{DX_{0.75}M}$ samples in the adsorption of Cr^{6+} solution at 300 ppm.

6.4.2 Chromium (Cr^{6+}) adsorption kinetic studies

Chromium (Cr^{6+}) adsorption kinetic was evaluated in the pseudo-first and pseudo-second-order rate equations according to *Equation 7 and 8*, respectively. For these analyses, chromium (Cr^{6+}) adsorption kinetics were studied in $Q_{DX_{0.75}M}$ samples exposed at 300 ppm chromium solutions, at 1:1 mL of solution: mg of hydrogel ratio. The experiments were developed at temperatures of 25°C, 35°C, and 45°C, at pH 7, and the absorbance was measure in several time intervals until equilibrium was reached.

The results of the pseudo-first and pseudo-second-order kinetic plots for Chromium (Cr^{6+}) are expressed in *Figure 16* (a-c). From the pseudo-first and pseudo-second-order fitting, and with the use of Origin as a digital software to solve non-linear regressions, it was possible to obtain the kinetic constants, k_1 , k_2 , the theoretical amount of Cr^{6+} adsorbed (q_e), and the regression coefficients R^2 for the kinetic fitting models obtained. These results are present in *Table 5*.

From the kinetic constants, it can be inferred that the well-fitted adsorption kinetics is the pseudo-first-order kinetics whose regression coefficients (R^2) are 0.9961, 0.9942, and 0.9802 for the 25 °C, 35 °C, and 45 °C temperatures, which points out a physisorption process as a predominant step for the chromium Cr^{6+} adsorption on $Q_{DX_{0.75}M}$ samples. This is

corroborated with the theoretical maximum adsorption capacity (q_e) values of the pseudo-first-order model, which are closer to the experimental q_e values.

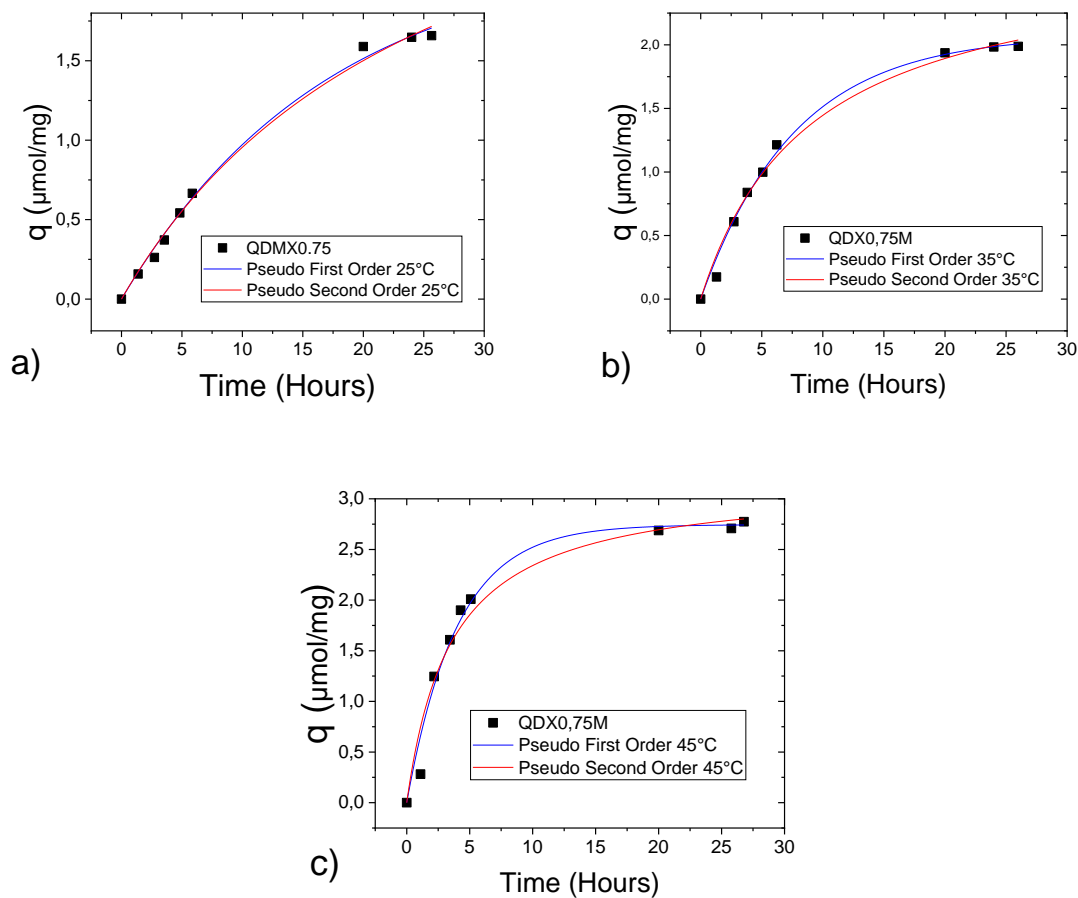


Figure 16. Pseudo first and pseudo second order kinetic plots for Cr^{6+} adsorption on $\text{QDX}_{0.75}\text{M}$ samples at a) 25 °C, b) 35 °C and c) 45 °C.

It is also observed that the kinetic rate constant k_1 increases with the increase in temperature, which indicates that the kinetic adsorption process is favored with the temperature rising.

Table 5. Kinetic parameters for Cr^{6+} adsorption on $QDX_{0.75}M$ samples at 25 °C, 35 °C and 45 °C.

Kinetic constants	25 °C	35 °C	45 °C
Pseudo First Order			
$q_e (exp)$ [umol/mg]	1.6578	1.9883	2.7733
$q_e (calc)$ [umol/mg]	2.1963	2.0772	2.7452
k_1 [min^{-1}]	0.0584	0.1305	0.2508
R^2	0.9961	0.9942	0.9802
Pseudo Second Order			
$q_e (calc)$ [umol/mg]	3.4935	2.7411	3.1739
k_2 [min^{-1}]	0.0108	0.0407	0.0885
R^2	0.9950	0.9906	0.9669

Intraparticle diffusion analysis.

The intraparticle diffusion model was plotted by the *Equation 9* from the 2.6 section of this work. **Figure 17** shows the intraparticle diffusion model by plotting the amount adsorbed qt versus $t^{1/2}$ for different temperatures. All the curves show a similar behavior having an initial curved part which corresponds to a bulk diffusion or external surface adsorption, followed by a gradual adsorption stage represented by the linear portion of the plot, which refers to the intraparticle diffusion, and finally, the equilibrium stage where intraparticle diffusion starts to slow down [92]. This behavior represents the intraparticle uptake of Chromium (Cr^{6+}) into the adsorbate and the pore diffusion in the adsorption [93].

From the linear part of the plots were possible to analyze the intraparticle diffusion process, and the results are synthesized in **Table 6**. The C constant obtained from the intercept of the linear fitting is different from zero, indicating that the intraparticle diffusion is not the only rate-limiting step involving another kinetic model, which may also control the adsorption rate [64]. On the other hand, C values are related to boundary diffusion or surface adsorption, which according to **Table 6**, increase while the temperature increases, indicating enhanced surface adsorption when temperature rises [94]. Similar effects are experienced by the intraparticle rate constants (k_d), with the increasing temperature boosting the intraparticle diffusion process.

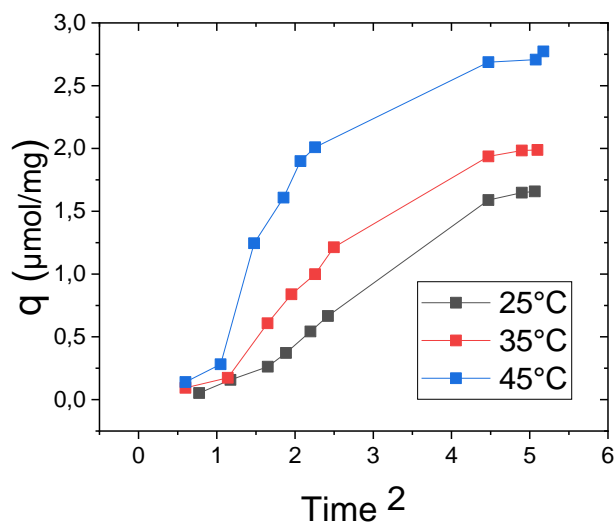


Figure 17. Intraparticle diffusion plots at different temperatures for Cr^{6+} adsorption on $QDX_{0.75}M$ samples.

Table 6. Intraparticle diffusion constants calculated at different temperatures for Cr^{6+} adsorption on $QDX_{0.75}M$ samples.

Intraparticle Diffusion	25°C	35°C	45°C
k_d [$\mu\text{mol}/\text{mg}\cdot\text{min}^{-1}$]	0.5276	0.6921	1.0151
C [$\mu\text{mol}/\text{mg}$]	-0.6151	-0.5310	-0.2523
R^2	0.9995	0.9959	0.9945

6.4.3 Chromium (Cr^{6+}) adsorption equilibrium studies

Adsorption equilibrium studies provide helpful information for understanding adsorption mechanisms by interpreting isotherm systems in the adsorption process. Several isotherm linear models have been developed to find the most approximate fitting adsorption model to try to predict the distribution of adsorbates, to provide information about the adsorption mechanisms involved, to analyze the possible interactions between adsorbate and adsorbent, and to establish an isotherm adsorption model based on theoretical assumptions [61].

For the adsorption equilibrium experiments were analyzed mainly four adsorption models: the Langmuir, Freundlich, Redlich-Peterson, and Temkin equations. In the Langmuir model, monolayer adsorption is assumed, where the adsorbent has a homogeneous surface and uniform energy. With the Freundlich isotherm model, the adsorption process is assumed

for heterogeneous surfaces, considering multilayer adsorption and non-uniform energy distribution. The Redlich-Peterson isotherm model combines both Langmuir and Freundlich assumptions for a wide range of concentrations being applied not only for homogeneous systems but also for heterogeneous systems. Finally, the Temkin isotherm model is related to the indirect adsorbate-adsorbate interactions and the dependency of the heat of adsorption with the surface coverage in the adsorption process [95]. The equations for Langmuir, Freundlich, Temkin, and Redlich-Peterson, models are represented in the *equation 2, 4, 5, and 6* from the 2.6 section of this work, respectively.

For the adsorption experiments, several Q_DX_{0.75}M samples were immersed into Cr⁶⁺ solutions at 100, 150, 200, 250, 300, 400, 800, and 1000 ppm concentrations and at 1:1 mL of solution: mg of hydrogel ratio. The experiments were carried out at temperatures of 25 °C, 35 °C, and 45 °C, and pH 7 in batch systems with a contact time of 24 hr, measuring the “q_e” values at the equilibrium. The non-linear models for Langmuir, Freundlich, Redlich-Peterson, and Temkin models for the isothermal adsorption of Cr⁶⁺ are shown in **Figure 18** (a-c), **Figure 19** (a-c), **Figure 20** (a-c), **Figure 21** (a-c), respectively. To obtain the Langmuir, Freundlich, Redlich Peterson, and Temkin adsorption isotherm fittings and equilibrium constants, a digital software “Origin” was used to find the well fitted non-linear regressions for the Chromium (Cr⁶⁺) adsorption on Q_DX_{0.75}M samples at different temperatures. **Table 7** exposes the calculated isotherm parameters for the Langmuir, Freundlich, Redlich Peterson, and Temkin models at 25 °C, 35 °C, and 45 °C temperatures.

From the results, it can be inferred that the Redlich Peterson isotherm is the best-fitted adsorption isotherm to describe the Chromium (Cr⁶⁺) adsorption mechanisms which are reflected on the regression coefficient values ($R^2=0.9968$, 0.9665 , and 0.9746 for the 25 °C, 35 °C and 45 °C respectively), compared to the other evaluated isotherm models. The Redlich-Peterson exponential constant “n” lies between 0 and 1 for the temperatures of 25 ° and 35 °C, which indicates a good correlation in the model adsorption over these temperatures[96]. Based on these assumptions, it can be concluded that the type of adsorption does not follow ideal monolayer adsorption and combines both homogeneous and heterogeneous adsorption behavior [97].

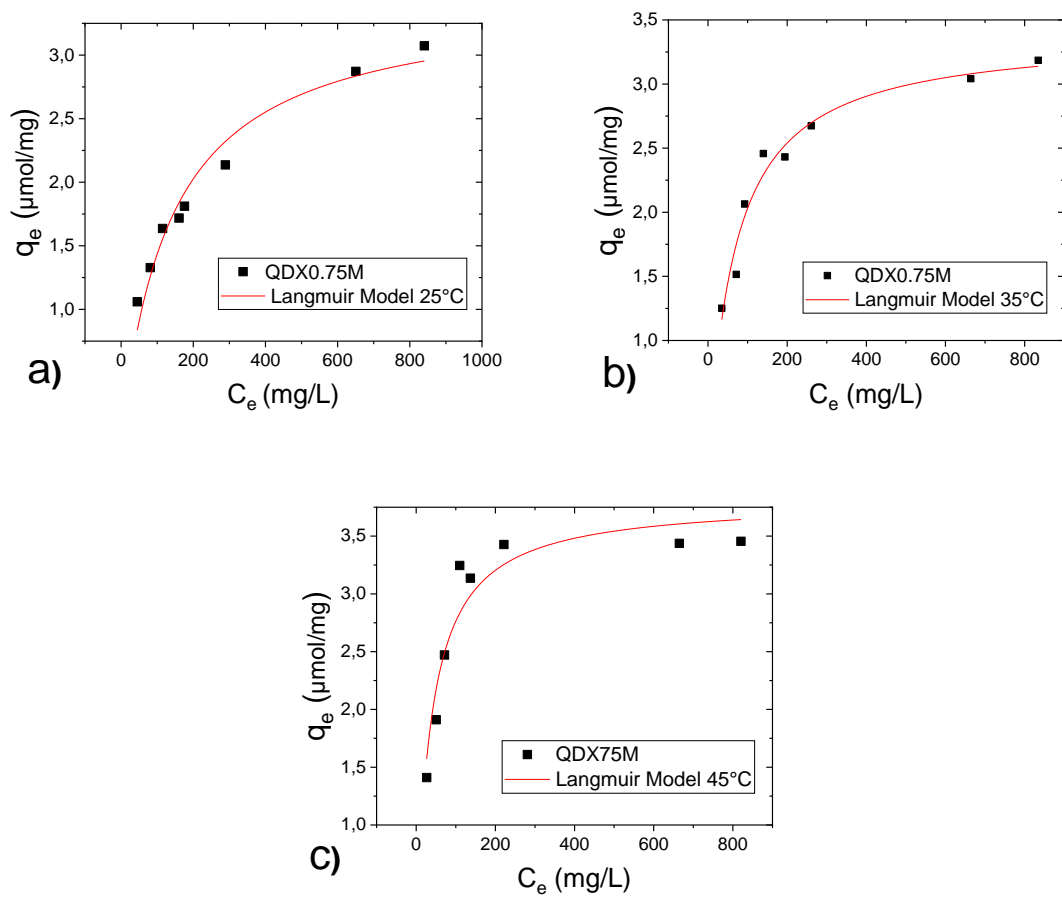
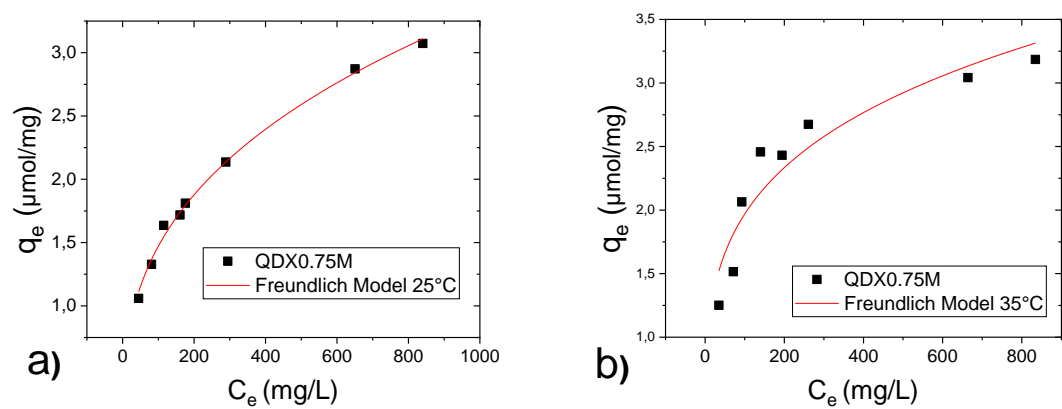


Figure 18. Langmuir isotherm plots for Cr^{6+} adsorption of $QDX_{0.75}M$ samples at a) 25 °C, b) 35 °C and c) 45 °C.



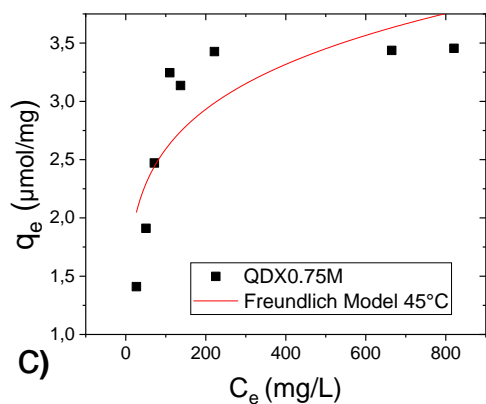


Figure 19. Freundlich isotherm plots for Cr^{6+} adsorption of $QDX_{0.75}M$ samples at a) 25 °C, b) 35 °C and c) 45 °C.

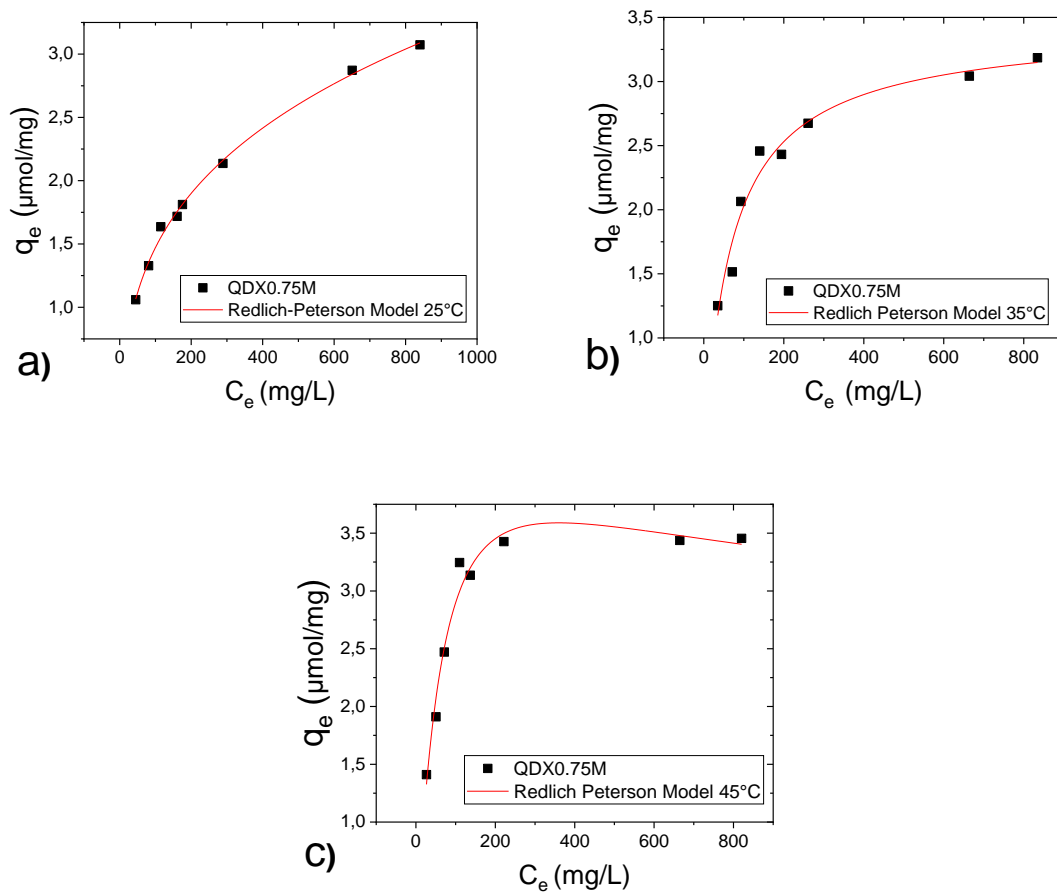


Figure 20. Redlich-Peterson isotherm plots for Cr^{6+} adsorption of $QDX_{0.75}M$ samples at a) 25 °C, b) 35 °C, and c) 45 °C.

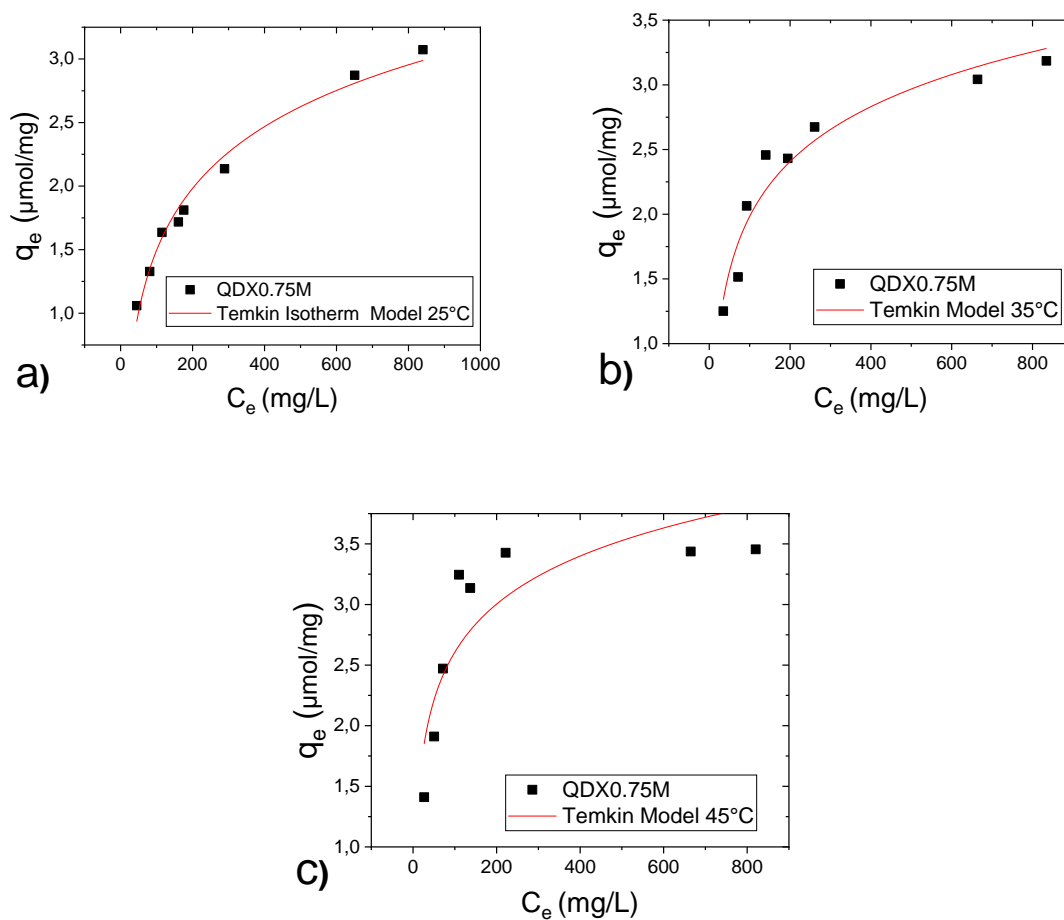


Figure 21. Temkin isotherm plots for Cr^{6+} adsorption of $QDX_{0.75}M$ samples at a) $25^{\circ}C$, b) $35^{\circ}C$ and c) $45^{\circ}C$.

It is also observed that a close relationship between the Langmuir and Redlich-Peterson fits when the “n” constant on the Redlich-Peterson model is closer to 1, which indicates that the Langmuir adsorption model behavior predominates over the Freundlich adsorption isotherm in the Redlich-Peterson isotherm model [98]. Furthermore, the separation factor “ R_L ” of the Langmuir isotherm model was calculated by the *Equation 3*, and the results are exposed in **Table 8**. It can be observed that all the “ R_L ” values are in the range of $0 < R_L < 1$, which indicates that the adsorption process is favorable and there is an affinity between adsorbate-adsorbent [98].

Table 7. Isotherm constants from Langmuir, Freundlich, Temkin, and Redlich-Peterson models at different temperatures, obtained from Cr^{6+} adsorption on $QDX_{0.75}M$ samples.

<i>Isotherm Constants</i>		<i>Temperature</i>		
		<i>25°C</i>	<i>35°C</i>	<i>45°C</i>
<i>Langmuir Isotherm Model</i>	<i>K_l</i>	0.0071	0.0149	0.0263
	<i>q_m</i>	3.4469	3.3904	3.8117
	<i>R²</i>	0.9610	0.9664	0.9119
<i>Freundlich Isotherm Model</i>	<i>K_f</i>	0.2917	0.6361	1.1403
	<i>n</i>	2.8456	4.0755	5.6105
	<i>R²</i>	0.9956	0.8930	0.6761
<i>Temkin Isotherm Model</i>	<i>B</i>	0.7014	0.6119	0.5720
	<i>A</i>	0.0844	0.2555	0.9530
	<i>R²</i>	0.9835	0.9404	0.7531
<i>Redlich Peterson Isotherm Model</i>	<i>K_r</i>	0.1344	0.0526	0.0611
	<i>a</i>	0.3341	0.0169	0.0045
	<i>n</i>	0.6932	0.9875	1.1952
	<i>R²</i>	0.9968	0.9665	0.9746

Table 8. Separation factor from Langmuir Models at different temperatures.

<i>C₀ [ppm]</i>	<i>R_L values</i>		
	<i>25°C</i>	<i>35°C</i>	<i>45°C</i>
100	0.5848	0.4016	0.2755
150	0.4843	0.3091	0.2022
200	0.4132	0.2513	0.1597
250	0.3604	0.2116	0.1320
300	0.3195	0.1828	0.1125
400	0.2604	0.1437	0.0868
800	0.1497	0.0774	0.0454
1000	0.1235	0.0629	0.0366

6.4.4 Chromium (Cr⁶⁺) adsorption thermodynamic studies

For the chromium (Cr⁶⁺) adsorption thermodynamic analysis, the Gibbs free energy, (ΔG° [kJ/mol]), enthalpy (ΔH° [Kj/mol]), and entropy change (ΔS° [kJ/mol*K]) were calculated using Equation 10, 11, and 12, respectively, and the results are exposed on **Table 9**.

Table 9. Thermodynamic parameters for Chromium (Cr⁶⁺) adsorption into QDX_{0.75M} samples.

<i>T [K]</i>	<i>LnK</i>	<i>ΔG° [kJ/mol]</i>	<i>ΔH° [Kj/mol]</i>	<i>ΔS° [kJ/mol*K]</i>
298	-7.81	-75.69	-47.76	0.09040
308	-7.55	-76.63		
318	-6.58	-77.57		

The results present negative values for ΔG° and ΔH° are negative, and the value of ΔS° is positive. The negative values for ΔG° indicate the reaction's feasibility and the favored adsorption's spontaneous nature with an increasing trend in the adsorption feasibility of Chromium (Cr^{6+}) with temperature. The negative value for ΔH° indicates the exothermic nature of the adsorption. Finally, the positive ΔS° value suggests an increased entropy in the solid-solution interaction and interface adsorption during the Chromium (Cr^{6+}) adsorption in $\text{QD}_{0.75}\text{M}$ samples [93].

7 CONCLUSIONS AND RECOMMENDATIONS

CS Based hydrogels nanocomposites previously prepared by drip method with glutaraldehyde as a crosslinking agent and magnetic nanoparticles have been characterized and evaluated for the adsorption of metal ions in waste-water treatment. SEM and TEM micrographs' morphological and structural analysis demonstrates a successful impregnation of magnetite in the crosslinked chitosan matrix. It is noticeable that the presence of magnetite on CS-based hydrogels changes their morphology by increasing the pore sizes, showing pores with regular and well-defined shapes, while the crosslinking presence seems to have no significant influence on the pore structure. On the other hand, the compositional analysis made by the FTIR and XPS techniques confirms the interactions between crosslinking-chitosan-magnetite molecules. For the FTIR chitosan hydrogels spectra, the observed bands around 3400 cm^{-1} and 560 cm^{-1} related to Fe-O interactions confirm magnetite's presence, and the increased bands at 2920 cm^{-1} and 1654 cm^{-1} related to C-H and C=N interactions confirms an existing crosslinking in the chitosan structure. With the XPS spectra analysis also was possible to find binding energies associated with O1s, N1s, and C1s orbitals and especially those found at 710 e.V and 724 e.V, which are present only on magnetic chitosan samples, corresponding to Fe $2p_{1/2}$ and Fe $3/2$ orbitals, confirming the embedded magnetic nanoparticles on the hydrogel surface. On the other hand, swelling experiments determine that the behavior depends on the crosslinking degree, magnetite presence, pH, and temperature. CS-based hydrogels reach the swelling equilibrium at 60 min, decreasing their swelling degree when the crosslinking degree and magnetic nanoparticles increase. CS-based hydrogels show an increased swelling behavior at more acid or basic mediums and increased temperature. Finally, adsorption experiments showed a maximum adsorption quantity of Chromium (Cr^{6+}) adsorbed was $1,8117\text{ }\mu\text{mol/mg}$, at standard conditions (pH 7, $25\text{ }^{\circ}\text{C}$) by QD \times 0.75M sample with a contact time of 24 hrs. The adsorption capacity increases at low pH solutions and with the increase in temperature. The kinetic adsorption process was better fitted by the pseudo-second-order kinetic. The Redlich-Peterson resulted in the best isotherm fitting with the high correlation coefficients than the Langmuir, Freundlich, and Temkin isotherms, indicating that the adsorption mechanism is a mix of both Langmuir and Freundlich models with a predominant Langmuir behavior, following non-ideal monolayer adsorption on the surface of the magnetic adsorbents. These aspects evidence a satisfactory

performance of CS-based hydrogel nanocomposites in the Chromium (Cr^{6+}) removal as an adsorption material used for waste-water treatment.

For future research on this topic, it is recommended to test the adsorption process on the magnetic CS-nanocomposites hydrogels prepared by the solvating evaporated method and compare the results presented in this work. The implemented procedure in synthesizing magnetic chitosan hydrogels could play an essential role in the resulting adsorption capacity of the material, especially by the change in the morphology. Also, it is recommended to test the adsorption capacities of the evaluated magnetic CS-nanocomposites hydrogels prepared by the drip method with other metal ions to compare the adsorption efficiency to other toxic metals. Finally, it is recommended for future work on this research to take this thesis project as a guide in developing new investigations in the use of chitosan as a biopolymer used to remove toxic metals in wastewaters.

8 BIBLIOGRAPHY:

- [1] V. Masindi and K. L. Muedi, “Environmental Contamination by Heavy Metals,” *Heavy Met.*, Jun. 2018, doi: 10.5772/INTECHOPEN.76082.
- [2] Y. Huang *et al.*, “An integrated approach to assess heavy metal source apportionment in peri-urban agricultural soils,” *J. Hazard. Mater.*, vol. 299, pp. 540–549, Dec. 2015, doi: 10.1016/J.JHAZMAT.2015.07.041.
- [3] J. Ren, P. N. Williams, J. Luo, H. Ma, and X. Wang, “Sediment metal bioavailability in Lake Taihu, China: evaluation of sequential extraction, DGT, and PBET techniques,” *Environ. Sci. Pollut. Res. 2015 2217*, vol. 22, no. 17, pp. 12919–12928, Apr. 2015, doi: 10.1007/S11356-015-4565-9.
- [4] G. K. Khadse, P. M. Patni, P. S. Kelkar, and S. Devotta, “Qualitative evaluation of Kanhan river and its tributaries flowing over central Indian plateau,” *Environ. Monit. Assess. 2007 1471*, vol. 147, no. 1, pp. 83–92, Dec. 2007, doi: 10.1007/S10661-007-0100-X.
- [5] Q. Zhou *et al.*, “Total concentrations and sources of heavy metal pollution in global river and lake water bodies from 1972 to 2017,” *Glob. Ecol. Conserv.*, vol. 22, p. e00925, Jun. 2020, doi: 10.1016/J.GECCO.2020.E00925.
- [6] L. Y *et al.*, “Trends and Health Risks of Dissolved Heavy Metal Pollution in Global River and Lake Water from 1970 to 2017,” *Rev. Environ. Contam. Toxicol.*, vol. 251, pp. 1–24, 2020, doi: 10.1007/398_2019_27.
- [7] S. Li and Q. Zhang, “Risk assessment and seasonal variations of dissolved trace elements and heavy metals in the Upper Han River, China,” *J. Hazard. Mater.*, vol. 181, no. 1–3, pp. 1051–1058, Sep. 2010, doi: 10.1016/J.JHAZMAT.2010.05.120.
- [8] F. Fu and Q. Wang, “Removal of heavy metal ions from wastewaters: A review,” *J. Environ. Manage.*, vol. 92, no. 3, pp. 407–418, Mar. 2011, doi: 10.1016/J.JENVMAN.2010.11.011.
- [9] K. C. Kemp *et al.*, “Environmental applications using graphene composites: water

- remediation and gas adsorption,” *Nanoscale*, vol. 5, no. 8, pp. 3149–3171, Mar. 2013, doi: 10.1039/C3NR33708A.
- [10] N. G. Burciaga-Montemayor *et al.*, “Compósitos en estado hidrogel con aplicación en la adsorción de metales pesados presentes en aguas residuales,” *TIP. Rev. Espec. en ciencias químico-biológicas*, vol. 23, pp. 1–13, Mar. 2020, doi: 10.22201/FESZ.23958723E.2020.0.211.
- [11] M. Vakili *et al.*, “Application of chitosan and its derivatives as adsorbents for dye removal from water and wastewater: A review,” *Carbohydr. Polym.*, vol. 113, pp. 115–130, Nov. 2014, doi: 10.1016/J.CARBPOL.2014.07.007.
- [12] G. Z. Kyzas and M. Kostoglou, “Green Adsorbents for Wastewaters: A Critical Review,” *Mater. 2014, Vol. 7, Pages 333-364*, vol. 7, no. 1, pp. 333–364, Jan. 2014, doi: 10.3390/MA7010333.
- [13] G. A. F. Roberts, *Chitin Chemistry*. Macmillan Education UK, 1992.
- [14] E. P. A. Sanford, G. Skjak-Braek, T. Anthonsen and P. A. Sanford, “Chitin and Chitosan-Sources, Chemistry, Biochemistry, Physical Properties and Applications,” *Elsevier Applied, London*, pp. 51–69, 1989, Accessed: Jul. 24, 2021. [Online]. Available: <https://www.scirp.org/reference/ReferencesPapers.aspx?ReferenceID=357023>.
- [15] G. Crini, G. Torri, E. Lichtfouse, G. Z. Kyzas, L. D. Wilson, and N. Morin-Crini, “Dye removal by biosorption using cross-linked chitosan-based hydrogels,” *Environ. Chem. Lett. 2019 174*, vol. 17, no. 4, pp. 1645–1666, Jul. 2019, doi: 10.1007/S10311-019-00903-Y.
- [16] T. Józwiak, U. Filipkowska, P. Szymczyk, and M. Zyśk, “Effect of the form and deacetylation degree of chitosan sorbents on sorption effectiveness of Reactive Black 5 from aqueous solutions,” *Int. J. Biol. Macromol.*, vol. 95, pp. 1169–1178, Feb. 2017, doi: 10.1016/J.IJBIOMAC.2016.11.007.
- [17] J. Li *et al.*, “Brilliant red X-3B uptake by a novel polycyclodextrin-modified magnetic cationic hydrogel: Performance, kinetics and mechanism,” *J. Environ. Sci.*,

vol. 89, pp. 264–276, Mar. 2020, doi: 10.1016/J.JES.2019.09.008.

- [18] C. Zhang *et al.*, “Facile preparation of polyacrylamide/chitosan/Fe₃O₄ composite hydrogels for effective removal of methylene blue from aqueous solution,” *Carbohydr. Polym.*, vol. 234, p. 115882, Apr. 2020, doi: 10.1016/J.CARBPOL.2020.115882.
- [19] N. E. Valderruten, J. D. Valverde, F. Zuluaga, and E. Ruiz-Durántez, “Synthesis and characterization of chitosan hydrogels cross-linked with dicarboxylic acids,” *React. Funct. Polym.*, vol. 84, pp. 21–28, Nov. 2014, doi: 10.1016/J.REACTFUNCTPOLYM.2014.08.006.
- [20] H. V. Tran, L. D. Tran, and T. N. Nguyen, “Preparation of chitosan/magnetite composite beads and their application for removal of Pb(II) and Ni(II) from aqueous solution,” *Mater. Sci. Eng. C*, vol. 30, no. 2, pp. 304–310, Jan. 2010, doi: 10.1016/J.MSEC.2009.11.008.
- [21] M. W. Wan, C. C. Kan, B. D. Rogel, and M. L. P. Dalida, “Adsorption of copper (II) and lead (II) ions from aqueous solution on chitosan-coated sand,” *Carbohydr. Polym.*, vol. 80, no. 3, pp. 891–899, May 2010, doi: 10.1016/J.CARBPOL.2009.12.048.
- [22] M. V. Dinu and E. S. Dragan, “Evaluation of Cu²⁺, Co²⁺ and Ni²⁺ ions removal from aqueous solution using a novel chitosan/clinoptilolite composite: Kinetics and isotherms,” *Chem. Eng. J.*, vol. 160, no. 1, pp. 157–163, May 2010, doi: 10.1016/J.CEJ.2010.03.029.
- [23] R. M. Michell Uribe, F. A. López González, and M. G. López Aveiga, “Chitosan based hydrogel for wastewater treatment,” Yachay Tech.
- [24] N. A. Peppas and A. S. Hoffman, “Hydrogels,” *Biomater. Sci.*, pp. 153–166, Jan. 2020, doi: 10.1016/B978-0-12-816137-1.00014-3.
- [25] A. Hillebrecht *et al.*, *Modern superabsorbent polymer technology*. . New York, 2011.
- [26] E. M. Ahmed, “Hydrogel: Preparation, characterization, and applications: A review,”

J. Adv. Res., vol. 6, no. 2, pp. 105–121, Mar. 2015, doi:
10.1016/J.JARE.2013.07.006.

- [27] M. Bahram, N. Mohseni, and M. Moghtader, “An Introduction to Hydrogels and Some Recent Applications,” in *Emerging Concepts in Analysis and Applications of Hydrogels*, Technical Editor., Sutapa Biswas Majee, Ed. 2016, pp. 9–10.
- [28] W. Wang, R. Narain, and H. Zeng, “Hydrogels,” *Polym. Sci. Nanotechnol.*, pp. 203–244, Jan. 2020, doi: 10.1016/B978-0-12-816806-6.00010-8.
- [29] T.-C. Tseng, L. Tao, F.-Y. Hsieh, Y. Wei, I.-M. Chiu, and S. Hsu, “An Injectable, Self-Healing Hydrogel to Repair the Central Nervous System,” *Adv. Mater.*, vol. 27, no. 23, pp. 3518–3524, Jun. 2015, doi: 10.1002/ADMA.201500762.
- [30] S. Gennen *et al.*, “Polyhydroxyurethane hydrogels: Synthesis and characterizations,” *Eur. Polym. J.*, vol. 84, pp. 849–862, Nov. 2016, doi:
10.1016/J.EURPOLYMJ.2016.07.013.
- [31] V. H, B. L, L. P, and M. AP, “Nanocellulose-Based Materials for Water Purification,” *Nanomater. (Basel, Switzerland)*, vol. 7, no. 3, Mar. 2017, doi:
10.3390/NANO7030057.
- [32] T. H. Tran, H. Okabe, Y. Hidaka, and K. Hara, “Removal of metal ions from aqueous solutions using carboxymethyl cellulose/sodium styrene sulfonate gels prepared by radiation grafting,” *Carbohydr. Polym.*, vol. 157, pp. 335–343, Feb. 2017, doi: 10.1016/J.CARBPOL.2016.09.049.
- [33] V. Sinha and S. Chakma, “Advances in the preparation of hydrogel for wastewater treatment: A concise review,” *J. Environ. Chem. Eng.*, vol. 7, no. 5, p. 103295, Oct. 2019, doi: 10.1016/J.JECE.2019.103295.
- [34] A. A. Aly and M. K. El-Bisi, “Grafting of Polysaccharides: Recent Advances,” *Biopolym. Grafting Synth. Prop.*, pp. 469–519, Jan. 2018, doi: 10.1016/B978-0-323-48104-5.00011-1.
- [35] P. Yu *et al.*, “Self-Assembled Sponge-like Chitosan/Reduced Graphene Oxide/Montmorillonite Composite Hydrogels without Cross-Linking of Chitosan for

- Effective Cr(VI) Sorption,” *ACS Sustain. Chem. Eng.*, vol. 5, no. 2, pp. 1557–1566, Feb. 2017, doi: 10.1021/ACSSUSCHEMENG.6B02254.
- [36] M. Khan and I. M. C. Lo, “Removal of ionizable aromatic pollutants from contaminated water using nano γ -Fe₂O₃ based magnetic cationic hydrogel: Sorptive performance, magnetic separation and reusability,” *J. Hazard. Mater.*, vol. 322, pp. 195–204, Jan. 2017, doi: 10.1016/J.JHAZMAT.2016.01.051.
- [37] G. Zhang, Y. Chen, Y. Deng, T. Ngai, and C. Wang, “Dynamic Supramolecular Hydrogels: Regulating Hydrogel Properties through Self-Complementary Quadruple Hydrogen Bonds and Thermo-Switch,” *ACS Macro Lett.*, vol. 6, no. 7, pp. 641–646, Jul. 2017, doi: 10.1021/ACSMACROLETT.7B00275.
- [38] A. Faghijnejad and H. Zeng, “Hydrophobic interactions between polymer surfaces: using polystyrene as a model system,” *Soft Matter*, vol. 8, no. 9, pp. 2746–2759, Feb. 2012, doi: 10.1039/C2SM07150A.
- [39] J. L. Holloway, A. M. Lowman, and G. R. Palmese, “The role of crystallization and phase separation in the formation of physically cross-linked PVA hydrogels,” *Soft Matter*, vol. 9, no. 3, pp. 826–833, Dec. 2012, doi: 10.1039/C2SM26763B.
- [40] K. K., “Chitin and chitosan: functional biopolymers from marine crustaceans,” *Mar. Biotechnol. (NY)*, vol. 8, no. 3, pp. 203–226, Jun. 2006, doi: 10.1007/S10126-005-0097-5.
- [41] A. Kangama, D. Zeng, X. Tian, and J. Fang, “Application of Chitosan Composite Flocculant in Tap Water Treatment,” *J. Chem.*, vol. 2018, 2018, doi: 10.1155/2018/2768474.
- [42] S. P. Chawla, S. R. Kanatt, and A. K. Sharma, “Chitosan,” in *Polysaccharides: Bioactivity and Biotechnology*, Springer Internatio..., K. G. M. J.-M. M. Ramawat, Ed. Springer, Cham, 2015, pp. 219–246.
- [43] R.-D. Park and J. Jung, “Enzymatic Production of Chitin from Crustacean Shell Waste,” in *Chitin, Chitosan, Oligosaccharides and Their Derivatives, Biological Activites and Applicationns*, Taylor & Francis G..., Se-Kwon Kim, Ed. 2010.

- [44] D. Elieh-Ali-Komi and M. R. Hamblin, "Chitin and Chitosan: Production and Application of Versatile Biomedical Nanomaterials," *Int. J. Adv. Res.*, vol. 4, no. 3, p. 411, Mar. 2016, Accessed: Aug. 06, 2021. [Online]. Available: </pmc/articles/PMC5094803/>.
- [45] R. F. Weska, J. M. Moura, L. M. Batista, J. Rizzi, and L. A. A. Pinto, "Optimization of deacetylation in the production of chitosan from shrimp wastes: Use of response surface methodology," *J. Food Eng.*, vol. 80, no. 3, pp. 749–753, Jun. 2007, doi: 10.1016/J.JFOODENG.2006.02.006.
- [46] M. N. V. Ravi Kumar, "A review of chitin and chitosan applications," *React. Funct. Polym.*, vol. 46, no. 1, pp. 1–27, Nov. 2000, doi: 10.1016/S1381-5148(00)00038-9.
- [47] M. Rhazi *et al.*, "Influence of the nature of the metal ions on the complexation with chitosan.: Application to the treatment of liquid waste," *Eur. Polym. J.*, vol. 38, no. 8, pp. 1523–1530, Aug. 2002, doi: 10.1016/S0014-3057(02)00026-5.
- [48] P. Mohammadzadeh Pakdel and S. J. Peighambaroust, "Review on recent progress in chitosan-based hydrogels for wastewater treatment application," *Carbohydr. Polym.*, vol. 201, pp. 264–279, Dec. 2018, doi: 10.1016/J.CARBPOL.2018.08.070.
- [49] M. S. Chiou, P. Y. Ho, and H. Y. Li, "Adsorption of anionic dyes in acid solutions using chemically cross-linked chitosan beads," *Dye. Pigment.*, vol. 60, no. 1, pp. 69–84, Jan. 2004, doi: 10.1016/S0143-7208(03)00140-2.
- [50] F. C. Wu, R. L. Tseng, and R. S. Juang, "Enhanced abilities of highly swollen chitosan beads for color removal and tyrosinase immobilization," *J. Hazard. Mater.*, vol. 81, no. 1–2, pp. 167–177, Jan. 2001, doi: 10.1016/S0304-3894(00)00340-X.
- [51] A. Anitha, S. N. Rejinold, J. D. Bumgardner, S. V. Nair, and R. Jayakumar, "Approaches for Functional Modification or Cross-Linking of Chitosan," in *Chitosan-Based Systems for Biopharmaceuticals: Delivery, Targeting and Polymer Therapeutics*, Jhon Wiley., B. Sarmento and J. Neves, Eds. John Wiley & Sons, Ltd, 2012, pp. 107–124.
- [52] A. Kamari, W. S. W. Ngah, M. Y. Chong, and M. L. Cheah, "Sorption of acid dyes

- onto GLA and H₂SO₄ cross-linked chitosan beads,” *Desalination*, vol. 249, no. 3, pp. 1180–1189, Dec. 2009, doi: 10.1016/J.DESAL.2009.04.010.
- [53] T. Józwiak, U. Filipkowska, J. Rodziejewicz, and E. Nowosad, “EFFECT OF CROSS-LINKING WITH GLUTARALDEHYDE ON ADSORPTION CAPACITY OF CHITOSAN BEADS,” *Prog. Chem. Appl. Chitin its Deriv.*, vol. 18, no. 18, pp. 35–47, 2013.
- [54] N. Islam, I. Dmour, and M. O. Taha, “Degradability of chitosan micro/nanoparticles for pulmonary drug delivery,” *Heliyon*, vol. 5, no. 5, p. e01684, May 2019, doi: 10.1016/J.HELIYON.2019.E01684.
- [55] F. R, A. EK, L. NA, and S. WJ, “Crosslinking metal nanoparticles into the polymer backbone of hydrogels enables preparation of soft, magnetic field-driven actuators with muscle-like flexibility,” *Small*, vol. 5, no. 3, pp. 383–388, Feb. 2009, doi: 10.1002/SMLL.200801091.
- [56] N. S. Satarkar and J. Z. Hilt, “Magnetic hydrogel nanocomposites for remote controlled pulsatile drug release,” *J. Control. Release*, vol. 130, no. 3, pp. 246–251, Sep. 2008, doi: 10.1016/J.JCONREL.2008.06.008.
- [57] O. Ozay, S. Ekici, Y. Baran, N. Aktas, and N. Sahiner, “Removal of toxic metal ions with magnetic hydrogels,” *Water Res.*, vol. 43, no. 17, pp. 4403–4411, Sep. 2009, doi: 10.1016/J.WATRES.2009.06.058.
- [58] E. Anastasova *et al.*, “A pure magnetite hydrogel: synthesis, properties and possible applications,” *Soft Matter*, vol. 13, no. 45, pp. 8651–8660, 2017, doi: 10.1039/C7SM01702B.
- [59] A. T. Paulino, L. A. Belfiore, L. T. Kubota, E. C. Muniz, V. C. Almeida, and E. B. Tambourgi, “Effect of magnetite on the adsorption behavior of Pb(II), Cd(II), and Cu(II) in chitosan-based hydrogels,” *Desalination*, vol. 275, no. 1–3, pp. 187–196, Jul. 2011, doi: 10.1016/J.DESAL.2011.02.056.
- [60] H. Mittal, A. Maity, and S. S. Ray, “The Adsorption of Pb²⁺ and Cu²⁺ onto Gum Ghatti-Grafted Poly(acrylamide-co-acrylonitrile) Biodegradable Hydrogel: Isotherms

- and Kinetic Models,” *J. Phys. Chem. A*, vol. 119, no. 5, pp. 2026–2039, Feb. 2015, doi: 10.1021/JP5090857.
- [61] N. Ayawei, A. N. Ebelegi, and D. Wankasi, “Modelling and Interpretation of Adsorption Isotherms,” *J. Chem. 2017, Vol. 2017, Pages 1-11*, vol. 2017, pp. 1–11, Sep. 2017, doi: 10.1155/2017/3039817.
- [62] V. Van Tran, D. Park, and Y.-C. Lee, “Hydrogel applications for adsorption of contaminants in water and wastewater treatment,” *Environ. Sci. Pollut. Res. 2018 2525*, vol. 25, no. 25, pp. 24569–24599, Jul. 2018, doi: 10.1007/S11356-018-2605-Y.
- [63] D. Ringot, B. Lerzy, K. Chaplain, J. P. Bonhoure, E. Auclair, and Y. Larondelle, “In vitro biosorption of ochratoxin A on the yeast industry by-products: Comparison of isotherm models,” *Bioresour. Technol.*, vol. 98, no. 9, pp. 1812–1821, Jul. 2007, doi: 10.1016/J.BIORTECH.2006.06.015.
- [64] T. Dula, K. Siraj, and S. A. Kitte, “Adsorption of Hexavalent Chromium from Aqueous Solution Using Chemically Activated Carbon Prepared from Locally Available Waste of Bamboo (*Oxytenanthera abyssinica*),” *ISRN Environ. Chem.*, vol. 2014, pp. 1–9, Feb. 2014, doi: 10.1155/2014/438245.
- [65] G. W. Kajjumba, S. Emik, A. Öngen, and H. K. Ö. and S. Aydın, “Modelling of Adsorption Kinetic Processes—Errors, Theory and Application,” *Adv. Sorption Process Appl.*, Nov. 2018, doi: 10.5772/INTECHOPEN.80495.
- [66] S. Kaur, S. Rani, and R. K. Mahajan, “Adsorption Kinetics for the Removal of Hazardous Dye Congo Red by Biowaste Materials as Adsorbents,” *J. Chem.*, 2013, doi: 10.1155/2013/628582.
- [67] Y. Bagbi, A. Sarswat, D. Mohan, A. Pandey, and P. R. Solanki, “Lead and Chromium Adsorption from Water using L-Cysteine Functionalized Magnetite (Fe₃O₄) Nanoparticles,” *Sci. Reports 2017 71*, vol. 7, no. 1, pp. 1–15, Aug. 2017, doi: 10.1038/s41598-017-03380-x.
- [68] B. Li *et al.*, “Synthesis, characterization, and antibacterial activity of cross-linked

- chitosan-glutaraldehyde,” *Mar. Drugs*, vol. 11, no. 5, pp. 1534–1552, 2013, doi: 10.3390/MD11051534.
- [69] D. Malwal and P. Gopinath, “Silica Stabilized Magnetic-Chitosan Beads for Removal of Arsenic from Water,” *Colloid Interface Sci. Commun.*, vol. 19, pp. 14–19, Jul. 2017, doi: 10.1016/J.COLCOM.2017.06.003.
- [70] M. Gierszewska, E. Jakubowska, and E. Olewnik-Kruszkowska, “Effect of chemical crosslinking on properties of chitosan-montmorillonite composites,” *Polym. Test.*, vol. 77, p. 105872, Aug. 2019, doi: 10.1016/J.POLYMERTESTING.2019.04.019.
- [71] X. Xiong, Y. Wang, W. Zou, J. Duan, and Y. Chen, “Preparation and characterization of magnetic chitosan microcapsules,” *J. Chem.*, 2013, doi: 10.1155/2013/585613.
- [72] X. Li, D. Zeng, P. Ke, G. Wang, and D. Zhang, “Synthesis and characterization of magnetic chitosan microspheres for drug delivery,” *RSC Adv.*, vol. 10, no. 12, pp. 7163–7169, Feb. 2020, doi: 10.1039/C9RA10792D.
- [73] J. C. Vickerman and I. S. Gilmore, “Surface Analysis - The Principal Techniques: Second Edition,” *Surf. Anal. - Princ. Tech. Second Ed.*, pp. 1–666, Mar. 2009, doi: 10.1002/9780470721582.
- [74] J. F. Moulder, W. F. Stickle, S. P.E., and K. D. Bomben, *Handbook of X-ray Photoelectron Spectroscopy*. Minnesota, 1995.
- [75] W. F. Yap, W. M. M. Yunus, Z. A. Talib, and N. A. Yusof, “X-ray photoelectron spectroscopy and atomic force microscopy studies on crosslinked chitosan thin film,” *Int. J. Phys. Sci.*, vol. 6, no. 11, pp. 2744–2749, Jun. 2011, doi: 10.5897/IJPS11.121.
- [76] T. M. Freire *et al.*, “Magnetic Porous Controlled Fe₃O₄–Chitosan Nanostructure: An Ecofriendly Adsorbent for Efficient Removal of Azo Dyes,” *Nanomater. 2020, Vol. 10, Page 1194*, vol. 10, no. 6, p. 1194, Jun. 2020, doi: 10.3390/NANO10061194.
- [77] B. Lindberg, R. Maripuu, K. Siegbahn, R. Larsson, C. G. Gölander, and J. C. Eriksson, “ESCA Studies of heparinized and related surfaces: 1. Model surfaces on

steel substrates,” *J. Colloid Interface Sci.*, vol. 95, no. 2, pp. 308–321, Oct. 1983, doi: 10.1016/0021-9797(83)90190-X.

- [78] L. Dambies, C. Guimon, S. Yiacoumi, and E. Guibal, “Characterization of metal ion interactions with chitosan by X-ray photoelectron spectroscopy,” *Colloids Surfaces A Physicochem. Eng. Asp.*, vol. 177, no. 2–3, pp. 203–214, Feb. 2001, doi: 10.1016/S0927-7757(00)00678-6.
- [79] Y. Tian, B. Yu, X. Li, and K. Li, “Facile solvothermal synthesis of monodisperse Fe₃O₄ nanocrystals with precise size control of one nanometre as potential MRI contrast agents,” *J. Mater. Chem.*, vol. 21, no. 8, pp. 2476–2481, Feb. 2011, doi: 10.1039/C0JM02913K.
- [80] X. Wang, H. Huang, G. Li, Y. Liu, J. Huang, and D.-P. Yang, “Hydrothermal synthesis of 3D hollow porous Fe₃O₄ microspheres towards catalytic removal of organic pollutants,” *Nanoscale Res. Lett. 2014 91*, vol. 9, no. 1, pp. 1–5, Nov. 2014, doi: 10.1186/1556-276X-9-648.
- [81] R. S. Vieira, M. L. M. Oliveira, E. Guibal, E. Rodríguez-Castellón, and M. M. Beppu, “Copper, mercury and chromium adsorption on natural and crosslinked chitosan films: An XPS investigation of mechanism,” *Colloids Surfaces A Physicochem. Eng. Asp.*, vol. 374, no. 1–3, pp. 108–114, Jan. 2011, doi: 10.1016/J.COLSURFA.2010.11.022.
- [82] C. Shen *et al.*, “Highly efficient detoxification of Cr(VI) by chitosan–Fe(III) complex: Process and mechanism studies,” *J. Hazard. Mater.*, vol. 244–245, pp. 689–697, Jan. 2013, doi: 10.1016/J.JHAZMAT.2012.10.061.
- [83] S. Zavareh, Z. Behrouzi, and A. Avanes, “Cu (II) binded chitosan/Fe₃O₄ nanocomposite as a new biosorbent for efficient and selective removal of phosphate,” *Int. J. Biol. Macromol.*, vol. 101, pp. 40–50, Aug. 2017, doi: 10.1016/J.IJBIOMAC.2017.03.074.
- [84] M. A. Agotegaray and V. L. Lassalle, “Study of the Experimental Conditions and Mechanisms for Diclofenac Loading in Functionalized Magnetic Nanoparticles,” *IJCPA*, vol. 1, no. 4, pp. 154–164, 2016, Accessed: Sep. 05, 2021. [Online].

Available: <https://ri.conicet.gov.ar/handle/11336/10367>.

- [85] Z. A. Sutirman, M. M. Sanagi, K. J. Abd Karim, and W. A. Wan Ibrahim, "Preparation of methacrylamide-functionalized crosslinked chitosan by free radical polymerization for the removal of lead ions," *Carbohydr. Polym.*, vol. 151, pp. 1091–1099, Oct. 2016, doi: 10.1016/J.CARBPOL.2016.06.076.
- [86] D. R. Rohindra, A. V Nand, and J. R. Khurma, "Swelling properties of chitosan hydrogels," *South Pacific J. Nat. Appl. Sci.*, vol. 22, no. 1, pp. 32–35, 2004, doi: 10.1071/SP04005.
- [87] A. L. Daniel-Da-Silva, J. Moreira, R. Neto, A. C. Estrada, A. M. Gil, and T. Trindade, "Impact of magnetic nanofillers in the swelling and release properties of κ -carrageenan hydrogel nanocomposites," *Carbohydr. Polym.*, vol. 87, no. 1, pp. 328–335, Jan. 2012, doi: 10.1016/J.CARBPOL.2011.07.051.
- [88] S. J. Kim, S. R. Shin, Y. M. Lee, and S. I. Kim, "Swelling characterizations of chitosan and polyacrylonitrile semi-interpenetrating polymer network hydrogels," *J. Appl. Polym. Sci.*, vol. 87, no. 12, pp. 2011–2015, Mar. 2003, doi: 10.1002/APP.11699.
- [89] M. Ghaemy and M. Naseri, "Synthesis of chitosan networks: Swelling, drug release, and magnetically assisted BSA separation using Fe₃O₄ nanoparticles," *Carbohydr. Polym.*, vol. 90, no. 3, pp. 1265–1272, Oct. 2012, doi: 10.1016/J.CARBPOL.2012.06.069.
- [90] R. Hua and Z. Li, "Sulfhydryl functionalized hydrogel with magnetism: Synthesis, characterization, and adsorption behavior study for heavy metal removal," *Chem. Eng. J.*, vol. 249, pp. 189–200, Aug. 2014, doi: 10.1016/J.CEJ.2014.03.097.
- [91] J. Sangeetha and J. Philip, "Synthesis, characterization and antimicrobial property of Fe₃O₄-Cys-HNQ nanocomplex, with L-cysteine molecule as a linker," *RSC Adv.*, vol. 3, no. 21, pp. 8047–8057, May 2013, doi: 10.1039/C3RA00005B.
- [92] C. K. Jain, D. C. Singhal, and M. K. Sharma, "Adsorption of zinc on bed sediment of River Hindon: adsorption models and kinetics," *J. Hazard. Mater.*, vol. 114, no. 1–3,

pp. 231–239, Oct. 2004, doi: 10.1016/J.JHAZMAT.2004.09.001.

- [93] S. Raghav and D. Kumar, “Adsorption Equilibrium, Kinetics, and Thermodynamic Studies of Fluoride Adsorbed by Tetrametallic Oxide Adsorbent,” *J. Chem. Eng. Data*, vol. 63, no. 5, pp. 1682–1697, May 2018, doi: 10.1021/ACS.JCED.8B00024.
- [94] A. Pholosi, E. B. Naidoo, and A. E. Ofomaja, “Intraparticle diffusion of Cr(VI) through biomass and magnetite coated biomass: A comparative kinetic and diffusion study,” *South African J. Chem. Eng.*, vol. 32, pp. 39–55, Apr. 2020, doi: 10.1016/J.SAJCE.2020.01.005.
- [95] M. del R. Sun-Kou, D. Obregón-Valencia, Á. Pinedo-Flores, A. L. Paredes-Doig, and J. Aylas-Orejón, “ADSORCIÓN DE METALES PESADOS EMPLEANDO CARBONES ACTIVADOS PREPARADOS A PARTIR DE SEMILLAS DE AGUAJE,” *Rev. la Soc. Química del Perú*, vol. 80, no. 4, pp. 225–236, Dec. 2014, doi: 10.37761/RSQP.V80I4.159.
- [96] S. J. Tshemese, W. Mhike, and S. M. Tichapondwa, “Adsorption of phenol and chromium (VI) from aqueous solution using exfoliated graphite: Equilibrium, kinetics and thermodynamic studies,” *Arab. J. Chem.*, vol. 14, no. 6, p. 103160, Jun. 2021, doi: 10.1016/J.ARABJC.2021.103160.
- [97] F. Brouers and T. J. Al-Musawi, “On the optimal use of isotherm models for the characterization of biosorption of lead onto algae,” *J. Mol. Liq.*, vol. 212, pp. 46–51, Dec. 2015, doi: 10.1016/J.MOLLIQ.2015.08.054.
- [98] N. T. R. N. Kumara, N. Hamdan, M. I. Petra, K. U. Tennakoon, and P. Ekanayake, “Equilibrium isotherm studies of adsorption of pigments extracted from Kuduk-kuduk (*Melastoma malabathricum* L.) pulp onto TiO₂ nanoparticles,” *J. Chem.*, vol. 2014, 2014, doi: 10.1155/2014/468975.